

**Quantum Chemical Calculations
on the Copper(II) Catalyzed
Michael Reaction**

Julia Borowka

Februar 2007

Quantum Chemical Calculations on the Copper(II) Catalyzed Michael Reaction

vorgelegt von Diplom-Chemikerin Julia Borowka
aus Bromberg/Polen

Der Fakultät II
–Mathematik und Naturwissenschaften, Institut für Chemie–
der Technischen Universität Berlin
zur Erlangung des akademischen Grades
Doktor der Naturwissenschaften
–Dr. rer. nat.–

genehmigte Dissertation

Promotionsausschuss:

Vorsitzender: Prof. Dr. A. Grohmann

Berichter: Prof. Dr. C. van Wüllen

Berichter: Prof. Dr. J. Sauer

Tag der wissenschaftlichen Aussprache: 30.03.2007

Berlin 2007

D 83

Prof. Dr. Christoph van Wüllen danke ich für die Vergabe dieses interessanten Themas, die wertvolle Unterstützung und das tolle Arbeitsklima. Ich möchte dem gesamten Arbeitskreis von Professor Christoph van Wüllen danken und Heidi Grauel insbesondere für die stetige Hilfsbereitschaft. Prof. Dr. Joachim Sauer danke ich für die Bereitschaft als zweiter Gutachter zu fungieren. Lüder Diedrich und Herrn Prof. Dr. Jens Christoffers danke ich für die Durchführung der Experimente und die gute diskussionsreiche Kooperation. Bei Francesco Fabbretti bedanke ich mich für die Durchführung der ESI-Massenspektroskopie. Dem *Konrad-Zuse-Zentrum* gegenüber bin ich Dankbar für die Zuteilung von Rechenzeit auf dem HLRN und Dr. Zoe Harvey mit Sandra Feyel für die Durchsicht von Teilen dieser Arbeit. Ein besonderer Dank gilt meiner Familie, Freunden und Christine Michauk.

Kurzzusammenfassung

Die vorliegende Dissertation befaßt sich mit dem Mechanismus der Kupfer(II)-katalysierten Michael-Reaktion von Enaminen, gebildet aus β -Diketonen und Aminosäuren, die an Methylvinylketone addieren. Wir präsentieren Ergebnisse zu möglichen Reaktionswegen und Komplexen unter Verwendung quantenchemischer Berechnungen (DFT) in enger Kooperation mit Experimentatoren. Wir zeigen, dass das Enamin nach Koordination an Cu(II) deprotoniert wird und drei Koordinationsstellen in der quadratisch planaren Geometrie besetzt. Die Bildung dieses koordinierten Aza-Enolats wird durch einen basischen co-Liganden (Azetat) begünstigt, der den Enamin-Wasserstoff übernimmt. In dieser starren Struktur steht die Aminosäure-Seitenkette senkrecht zu der Koordinationsebene, was zu einem Angriff des Michael-Akzeptors von der sterisch ungehinderten Seite bevorzugt und somit zum begünstigten Eantiomer führt, wenn von einem prochiralen Diketon ausgegangen wird. Die Diskriminierung wird dadurch ausgelöst, dass der Michael-Akzeptor an der freien axialen Position am Kupfer-Zentrum während der C-C-Knüpfung anbindet. Energien optimierter Übergangsstrukturen, die zu dem jeweiligen Eantiomer führen, wurden mit verschiedenen Aminosäuren (Methyl-, Isopropyl-, *tert*-Butyl und Neopentyl-Seitenkette) verglichen.

Übergangszustände, die zu den beiden Produkten führen, zeigen eine sehr unterschiedliche Struktur, da ein Angriff des Michael-Akzeptors von der sterisch ungünstigen Seite, eine Umorganisation der Koordinationssphäre am Kupfer-Zentrum auslöst. Interessanterweise ist der Reaktionsweg bei einem Angriff des Michael-Akzeptor von der sterisch ungünstigen Seite durch die Aminosäure blockiert. Eine Simulierung von Solvatationseffekten durch ein Kontinuum-Modell resultiert in einen Anstieg der Enantioselektivität mit zunehmender Polarität des Lösungsmittels.

Abstract

This PhD thesis concerns computational results on the mechanism of the copper(II) catalyzed Michael addition of enamines formed from β -diketones and amino acids. We present results on different paths and complexes feasible in the reaction using quantum chemical (DFT) calculations in comparison with experimental data. The results suggest that the enamine gets deprotonated upon coordination to Cu^{2+} , and that it occupies three coordination sites of a square planar geometry. The formation of this coordinated aza-enolate is facilitated by a basic co-ligand (acetate) which take over the enamine proton. In this rather rigid structure, the former amino acid side chain assumes an angular position which leads to preferred attack of the Michael acceptor from the non-hindered side of the coordination plane and the formation of a preferred enantiomer if one starts from a prochiral diketone. This discrimination becomes effective because the Michael acceptor, although only loosely bound to the complex before carbon-carbon bond formation, attaches itself to a "free" axial position of the copper center during the reaction. We focus on the enantioselectivity of the reaction by comparing energies of transition states which eventually lead to the formation of two enantiomers for amino acids (chiral auxiliaries) with a methyl, isopropyl, *tert*-butyl and neopentyl side chain. The transition states that lead to the two products are different in nature, because an approach of the Michael acceptor from the sterically hindered side requires reorganisation of the copper coordination sphere. Interestingly, this reaction channel is blocked by the amino acid side chain if the Michael acceptor approach from the less-hindered side. Taking solvent effects into account by a continuum solvation model, we find that the enantioselectivity increases with the polarity of the solvent, which is in agreement with experimental observations.

Contents

1	Introduction	1
1.1	The Michael Reaction	2
2	Theoretical background	7
2.1	Computational chemistry	7
2.2	Density Functional Theory	7
2.2.1	Local density approximation LDA	9
2.2.2	Beyond LDA: the generalized gradient approximation (GGA) and hybrid functionals	10
2.2.3	Calculation of the Coloumb term	12
2.2.4	Accuracy of the DFT method	13
2.2.5	Which exchange-correlation functional should be chosen?	14
2.3	Characterisations of chemical reactions	16
2.3.1	Geometry optimisation	17
2.3.2	Steepest Descent	17
2.3.3	Newton-Raphson	17
2.4	Transition states	19
2.5	Reaction pathways	21
2.6	Solvation models	22
3	Mechanism	25
3.1	The investigated reaction pathways	25
3.2	Metal-free background reaction	27
3.3	Nucleophilic attack through a coordinated enamine	29
3.4	Nucleophilic attack through a coordinated aza-enolate	32

3.4.1	Ligand effects in the C-C bond formation of a coordinated aza-enolate on copper(II)	35
3.5	Experimental proof of the mechanism: Non-reactivity of a secondary enamine?	37
3.6	Kinetics and Electro Spray Ionisation (ESI) mass spectroscopy	39
3.7	Solvent effects	41
3.8	Conclusion for the mechanism	45
4	Enantioselectivity	50
4.1	Calculation of enantioselectivity	50
4.2	Methods of Computation	51
4.2.1	L-Alanine (Ala) and L-valine (Val)	54
4.2.2	L- <i>tert</i> -Leucine (Tle) and L-neopentylglycine (Npg) . .	55
4.2.3	Comparison of the matched and mismatched transition state	57
4.3	Solvation effects on the enantioselectivity	61
4.4	Metal-free background reaction	65
5	Computational details	69
6	Summary	72
7	Tables	76
8	References	83
9	Appendix	92
9.1	Color code of Figures 3, 4, 5, 6, 7, 13, 16, 17, 18, 19, 20.	92
9.2	Absolute energies of the calculated structures	93

9.3	Overview of the calculated structures	98
9.4	List of Publications	104

List of Figures

1	First proposed structure of the reactive species by Christoffers et al.	4
2	Schematic representation of the Solvent Accessible Surface (SAS)	23
3	Transition state TS 3a/6 for C-C bond formation in the metal-free background reaction. Note that proton transfer from N to O occurs simultaneously.	28
4	Optimised transition state TS7a/8a of a coordinated enamine on copper (II).	30
5	Optimised structures investigated in different reaction pathways of the coordinated enamine on copper. Number in brackets show the relative energies in kJ/mol. Note that TS7c/8c doesn't lead to the desired product.	31
6	Transition state TS 9b/10b for C-C bond formation between a coordinated aza-enolate and the Michael acceptor. An acetic acid molecule serves as co-ligand.	36
7	Optimised transition state TS7d₄/8d for C-C bond formation of the secondary enamine coordinated on copper(II) (Here displayed in green) with two water co-ligands.	39
8	Result of the kinetics experiments showing the dependence of the relative kinetic constant on the catalyst concentration. Data: 6-ring-enamine 500mg (1,54 mmol) (0,154 mol/l), methylvinylketone 189 mg (2,70 mmol, 1,75 eq.), Cu(OAc) ₂ H ₂ O 0-7,5 mol, acetone 10 ml with 0,01 mol/l octanol as the reference.	40
9	ESI spectrum of the investigated system. Ratio between catalyst Cu(OAc) ₂ and enamine is 1:1 in the reaction mixture. . .	41
10	ESI spectrum of the fragment at 444 amu (C).	42

-
- 11 ESI spectrum of the fragment at 386 amu (**D**). 42
- 12 Investigated system in mass spectroscopy (ESI). 43
- 13 Transition state **TS-outside** of the outside attack of the Michael acceptor on the Michael donor with a high dipole moment . . . 45
- 14 Diagram of the calculated reaction barriers of inside attack and outside attack (study in gas phase and including solvent effects). 46
- 15 Energy profile of all investigated reaction pathways of the Michael addition mechanism. Note that these barriers include electronic energy without ZPVE. 49
- 16 Investigated reaction pathway of C-C bond formation. The preferred and the disfavoured attack of the coordinated aza-enolate on the Michael acceptor has been investigated. 59
- 17 Alternative transition state for the matched transition state **TS9a/10a** with a larger barrier than for the primer showed transition state for the favoured product. 60
- 18 This figure presents the optimised transition states. On the left side are the transition states for the matched and on the right side for the mismatched products. Left side: **TS9a/10a**, **TS9h/10h**. Right side: **TS9a/11a** **TS9h/11h**. 62
- 19 This figure presents the optimised transition states. On the left side are the transition states for the matched and on the right side for the mismatched products. Left side: **TS9i/10i**, **TS9j/10j**. Right side: **TS9i/11i**, **TS9j/11j**. 63

20	Optimised transition states of both product isomers using alanine and <i>tert.</i> -leucine as the chiral auxiliary. The favoured isomer both case is here the R isomer in contrast to the experimental data.	68
----	---	----

List of Tables

- 1 Reaction barriers of C-C bond formation (without zero-point vibrational energy (ZPVE)) of all investigated pathways of a coordinated aza-enolate on copper(II). 76
- 2 The first two columns contain solvation energies and the following three columns contain activation energies ($E(\text{TS}) - E(9a+4)$): [a], [b]: solvation energies calculated with the PCM and COSMO model, [c]: activation energies in gasphase, [d], [e]: activation energies calculated with the PCM and COSMO model 77
- 3 Reaction barriers differences ΔE_A (electronic energy without zero-point vibrational energy) (in kJ/mol) and derived enantioselectivity of several pathways using [a] different amino acids for the chiral auxiliaries using the B3LYP functional and TZVP basis set. 77
- 4 Results of the absolute reaction barriers using [a] different amino acids in the chiral auxiliaries in kJ/mol. TS describes the stereoisomer of the constructed product in the transition state. 78
- 5 C-C bond lengths for the optimised transition states of the matched and mismatched products using [a] different amino acids in the chiral auxiliaries. The results in the third column are without zero point vibrational energy correction (ZPVE) and the fourth column gives the reaction barrier with ZPVE. 78

6	Results of the out of plane angles of the square planar coordination sphere of copper(II) in the mismatched transition states with different amino acids. L means the type of ligands for the square planar coordination. Original means the four ligands are the aza-enolate and the water molecule. MA means that instead of the second ketone of the aza-enolate is the Michael acceptor 4 used as the ligand.	79
7	Calculated solvation energies (electronic energy without zero-point vibrational energy) [a] in kJ/mol using COSMO implemented in Gaussian out of the difference between a full COSMO optimisation and the gas phase result.	80
8	Reaction barriers (electronic energy without zero-point vibrational energy) differences of both stereo isomers ΔE_A and the resulting enantioselectivity using [a] different amino acids in the chiral auxiliaries, [b] in gas phase, [c] COSMO implemented in Gaussian [d] COSMO implemented in TURBO-MOLE using single point calculations compared to the experimental enantioselectivities.	81
9	Absolute reaction barriers (electronic energy without zero-point vibrational energy) for the pathways of both stereo isomers using [a] different amino acids in the chiral auxiliaries, in [b] gas phase and [c] COSMO using Gaussian03.	81
10	Results for the enantioselectivity of the C-C bond formation in the metal-free background reaction with different chiral auxiliaries . . .	82
11	Results of the absolute barriers [a]: gas phase and [b] using COSMO.	82

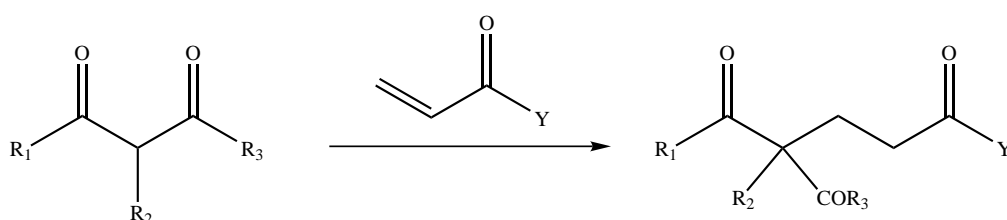
12	Absolute energies of different minima structures: [a] electronic energy and [b] the electronic energy plus the zero point vibrational energy correction calculated with Gaussian (assumption of classical behaviour for rotation in the frequency analysis).	93
13	Absolute energies of different transition states: [a] electronic energy and [b] the electronic energy plus the zero point vibrational energy correction calculated with Gaussian (assumption of classical behaviour for rotation in the frequency analysis).	96
14	Reduction of calculation time: Absolute energies in Hartree using the TZVP and the and SVP/SV basis set for two reaction pathways	97

1 Introduction

Formation of carbon-carbon bonds are the most important synthetic transformations in organic chemistry because this allows building complex molecules from simpler starting material [1–6]. Besides the aldol reaction [7], the Diels-Alder cycloaddition [8, 9] and the Heck reaction [10–13], the Michael addition [14–16] of carbon nucleophiles to acceptor-activated olefins belongs to the most popular C-C bond forming reactions. Being able to exert control such that only a specific product stereoisomer is formed is a major goal of synthetic organic chemistry. A particular challenge is the formation of one (and only one!) enantiomer of a chiral product from achiral starting material. A source of chiral information is of course needed, either through a chiral catalyst or a chiral auxiliary that is bound to the substrate stoichiometrically. In this work we investigate the Michael addition of an amino acid derivative of a 1,3-dicarbonyl compound to α, β -unsaturated ketones, catalyzed by Cu(II) salts. Quantum chemical (DFT) calculations have been performed to provide information on the mechanism of the reaction and how the chirality transfer from the chiral auxiliary to the product configuration comes effective. Insight into this reaction at molecular level is needed for further optimisation. For a model system, geometry optimisations of local minima (educts, products, and reaction intermediates) as well as transition structures have been performed for computing reaction channels and different chiral auxiliaries. This data is useful for discuss the factors which influence reactivity and selectivity of this system.

1.1 The Michael Reaction

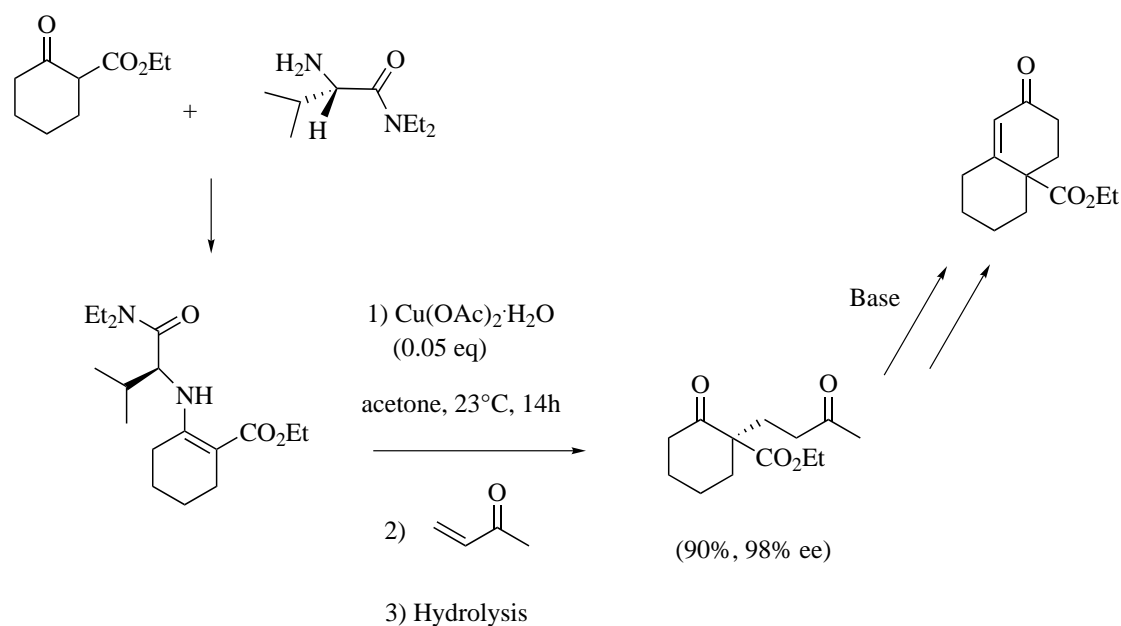
The conjugate 1,4-addition of carbon nucleophiles to acceptor activated olefins is one of the most important reactions in organic synthesis. This is mainly due to the variety of acceptors and donors (for example, organometallic reagents, enolates or enamines) applicable in this reaction (Scheme 1).



Scheme 1: General Michael reaction.

Carbanionic organolithium, Grignard reagent, copper, zinc, or other reagents are often utilized carbon nucleophiles. However, competing 1,2-addition to the acceptor is observed in the case of hard nucleophiles, especially when the acceptor is a carbonyl group. According to the Hard Soft Acid Base (HSAB) principle [17], organocuprates [18] are the classic reagents of choice for 1,4-reactivity. Whereas numerous publications deal with the formation of tertiary stereo centers by asymmetric cuprate additions, this method is rarely reported for the generation of quaternary carbon atoms. In particular, the copper-catalyzed addition of organo zinc reagents has evolved into a fruitful field of research since 2000 [18–20]. In contrast to organometallic compounds as nucleophiles, the application of derivatives with active methylene moieties (Michael donors) requires only catalytic amounts of Brønsted base, since the next equivalent of the donor is deprotonated by the enolate formed as intermediate immediately after conjugate addition of the donor to olefin. This reaction was first observed and reported by Kommenos and

Claisen [21, 22] and was later named after Arthur Michael [23–27] in order to honor his early systematic investigations. Asymmetric Michael reactions have been developed by several groups and are well suited to the highly selective construction of quaternary stereo centers [28–31].



Scheme 2: Cu(II)-catalyzed asymmetric Michael reaction with L-valine diethylamide as auxiliary [32–34].

Modern metal catalyzed variants allow for the use of base-free conditions [35, 36] to inhibit Robinson annelation, a base caused side reaction (Scheme 2). In 1999, Christoffers' group carried out an intensive screening program with several primary, chiral amines and transition metal salts as catalyst, which led to the development of a highly reliable process for the formation of quaternary stereo centers by Michael reactions [37, 38]. In their experiments they used the following system. L-Valine diethylamide combined with catalytic quantities of $\text{Cu}(\text{OAc})_2 \cdot \text{H}_2\text{O}$ turned out to be extraordinarily efficient

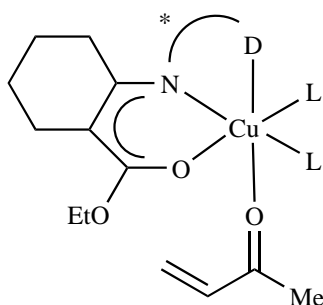
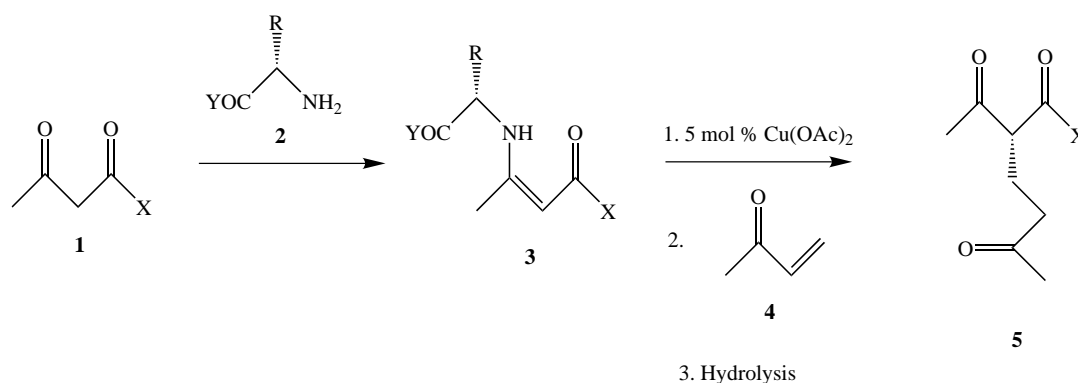


Figure 1: First proposed structure of the reactive species by Christoffers et al. .

for this purpose. The reaction of the conversion of enamines in the presence of $Cu(OAc)_2 \cdot H_2O$ (1-5 mol%) proceeds at ambient temperature. Anhydrous or inert condition are not required. The best solvent for this reaction in experiment is acetone. After acidic work up, the products were isolated in generally good yield, with selectivities up to 95–99% ee (Scheme 2). The auxiliary could be separated from the reaction mixture by extraction and recovered almost quantitatively. A special feature of the copper catalyzed reaction is the compatibility with different donor functions. Christoffers [39] first proposed an octahedral coordinated reactive species (Fig. 1) in the mechanism which was the starting point of our investigation.

In the iron catalyzed case [37, 40–42] it is furthermore clear from the outset that the nucleophile approaching the enone is a coordinated enolate, since the free diketone is no nucleophile and the free enolate cannot exist in sufficient concentration in the acidic reaction medium. In case of addition of enamines, the situation is more complicated: first, we will assume that the copper catalyzed enamine addition also involves a single copper site. Furthermore, there are three different possibilities as far as the nature of the nucleophile is concerned: first, the free enamine is nucleophilic enough to

add to enones, such that there will always be a non-catalyzed background reaction [39]. Then, there are two scenarios which involve a metal center: The enone is attacked by a coordinated enamine or by a coordinated aza-enolate. The latter is formed by deprotonation at the enamine nitrogen atom and is obviously a stronger nucleophile. However the question arises, if this species exists in sufficient quantities in the reaction medium to become important in the reaction. Enantioselectivity could be achieved starting from (chiral) enamines **3** made from β -diketones **1** and an amino acid derivative **2** which is used as a chiral auxiliary in stoichiometric quantities [32, 33, 39, 43–50](Scheme 3). Although the usefulness of this reaction has widely been demonstrated, experiments have so far contributed only limited insight into mechanistic details [33, 45–50]. In particular, it is not established how the chirality transfer from the auxiliary becomes effective. This situation triggered us to perform quantum chemical calculations to shed some light on the mechanism of this reaction



- 1a.** X=Me
2a. Y=NMe₂, R=Me
3a. X=Me, R=Me, Y=NMe₂

Scheme 3: Model system for computational studies.

In this PhD thesis, we first focus on the reaction mechanism, investigating which of the three pathways mentioned above, the most likely one is. Then we perform calculations on the enantioselectivity for the most likely mechanism. At the first stage, we also study solvent effects using continuum solvation models, both focusing on the reactivity and selectivity of the reaction. Calculations are based on density functional theory (DFT) because this method allows the treatment of transition metal catalyzed reactions with both a fair accuracy and a reasonable computational effort. Force field methods, which are much less expensive, have difficulties with a consistent description of breaking and forming of covalent bonds. Wave function based quantum chemistry on the other hand would require at least coupled cluster or even multi reference CI-type calculations with large basis sets for our system. These methods however require huge computational resources if more than say, two dozens of atoms are presented in the system. In the following part of the present thesis, we give a round overview.

2 Theoretical background

2.1 Computational chemistry

Computational chemistry can be defined as the application of theoretical chemistry which develop mathematical concepts to investigate chemical systems. There are three areas within computational chemistry devoted to the structure of molecules and their reactivity: molecular mechanics, electronic structure theory and DFT (density functional theory). DFT methods are used in many chemistry systems and in the calculations of this work.

2.2 Density Functional Theory

Density functional theory (DFT) [51] has gained popularity as a tool of quantum chemistry in the last twenty years. A clear indication of this was the Nobel Prize in Chemistry awarded to John Pople and Walter Kohn [52, 53]. Results from DFT calculations are usually superior to those from the Hartree-Fock method and often DFT can compete with correlated *ab initio* methods such as MP2. The great advantage of DFT is the possibility to get robust and accurate results for large molecules containing transition metals. The second advantage is the small calculation time required compared with wave function based methods including electron correlation.

The Hohenberg-Kohn-Theorem describes the energy of a system as a functional of the electron density ρ ;

$$E = F(\rho) \tag{1}$$

DFT based on the approximation of a functional determining the energy of a system as the electron density. The potential described through the nuclei of the atoms and the variational principle is imperative. The energy, written

as a functional of the wave function is

$$\langle \Psi | \hat{H} | \Psi \rangle = \langle \Psi | \hat{T} | \Psi \rangle + \langle \Psi | \hat{V} | \Psi \rangle + \sum_{i < j} \left\langle \Psi \left| \frac{1}{r_{i,j}} \right| \Psi \right\rangle \quad (2)$$

where the second term, describing the interaction with the external potential, can also be written as a functional of the density via

$$\langle \Psi | \hat{V} | \Psi \rangle = \int V(\vec{r}) \rho(\vec{r}) d\vec{r}. \quad (3)$$

The electron-electron interaction is calculated by equation 4 which consists of the *Hartree-Energy* and a second term, the *rest*, that includes the remaining energy:

$$\sum_{i < j} \left\langle \Psi \left| \frac{1}{r_{i,j}} \right| \Psi \right\rangle = \frac{1}{2} \int \left(\frac{\rho^{(1)} \rho^{(2)}}{r_{12}} \right) d\vec{r}_1 d\vec{r}_2 + rest = E_H(\rho) + rest \quad (4)$$

The kinetic energy is calculated using the following Kohn Sham method. Kohn and Sham introduced a functional for the calculation of the kinetic energy [53]. The expectancy value of the kinetic energy (equation 5) is calculated for all slater determinants which create the density $\rho(r)$. Then, the orbitals minimising the energy are selected.

$$E[\rho] = T_{KS}[\rho] + \int V \rho d\vec{r} + E_H[\rho] + E_{xc}[\rho] \quad (5)$$

$T_{KS}[\rho]$ is the kinetic energy calculated through the Kohn-Sham theory of a virtual system. Adding the potential energy $\int V \rho d\vec{r}$ and the Hartree energy with the important residue E_{xc} , the correlation exchange energy, we obtain the energy $E[\rho]$ of the system dependent on the density.

$$T_{KS}[\rho] = \text{Min}_{\Psi_{KS} \rightarrow \rho} \left\langle \Psi_{KS} \left| \hat{T} \right| \Psi_{KS} \right\rangle \quad (6)$$

Ψ_{KS} : single Slater Determinant

E_{xc} , the electron correlation exchange energy is defined as the difference between the accurate energy and the sum of Kohn-Sham and Hartree energy.

$$E_{xc} = (\langle \Psi | \hat{T} | \Psi \rangle - \langle \Psi | T_{KS} | \Psi \rangle) + (\sum_{i < j} \langle \Psi | \frac{1}{r_{i,j}} | \Psi \rangle - E_H[\rho]) \quad (7)$$

2.2.1 Local density approximation LDA

The simplest way to calculate correlation-exchange energy is described through the local density approximation (LDA) in eq. 8. Here is E_{xc} , at location \vec{r} , a function of the density $\rho(r)$,

$$E_{xc} = \int F_{xc}[\rho(\vec{r})] d\vec{r} \quad (8)$$

At Hartree-Fock level, the exchange energy (per volume unit) of a homogeneous electron gas, is given by

$$\epsilon_x = C_x \rho^{1/3} \quad (9)$$

$$E_x = \int C_x \rho^{4/3} d\vec{r} \quad (10)$$

$$E_{xc} = \int F_{xc}(\rho) d\vec{r} \quad (11)$$

where F_{xc} is a fitted function to the data of electron density calculated through Monte-Carlo simulation [54]. Due to these calculations we know the exchange-correlation density (ϵ_{xc}) of a homogeneous gas. To separate spin multiplicity we introduce the spin density.

$$E_{xc} = \int F_{xc}(\rho_\alpha, \rho_\beta) d\vec{r} \quad (12)$$

The LDA functional overestimates the binding energy (*over binding*). This can be improved by introducing gradient corrected functionals.

2.2.2 Beyond LDA: the generalized gradient approximation (GGA) and hybrid functionals

More sophisticated functionals use as additional information the spatial gradient of the electron density, $|\vec{\nabla}\rho|$. A general spin dependent and gradient developed density functional has the following definition:

$$E_{xc}^{GGA} = \int F_{xc}(\rho_\alpha, \rho_\beta, |\vec{\nabla}\rho_\alpha|^2, |\vec{\nabla}\rho_\beta|^2, \vec{\nabla}\rho_\alpha \vec{\nabla}\rho_\beta) d\vec{r} \quad (13)$$

In many cases, the function F_{xc} contains parameters that are fitted to experimental data, such that one may regard DFT as a semi empirical method. Technically, DFT and Hartree-Fock computer codes are very similar. The first gradient-corrected functional that was successfully applied to a variety of molecular problems was BP86, which improves upon LDA through gradient corrections to the exchange functional by Becke [55, 56] and to the correlation part by Perdew [57]. Calculated energy differences were now in much better agreement with experiment.

The next step forward was made when Becke suggested to include *exact exchange* (that is, a Fock term) into the energy expression. In *Hybrid functionals* part of the exchange energy calculated from the orbitals (rather the form of the density) uses the 'exact exchange' expression known from the Hartree-Fock-Theory.

$$E_X^{exact} = (ij|ji) = \int \int \chi_i(\vec{x}_1) \chi_j^*(\vec{x}_1) \frac{1}{r_{12}} \chi_j(\vec{x}_2) \chi_i^*(\vec{x}_2) d\vec{x}_1 d\vec{x}_2 \quad (14)$$

Functionals of this kind are called hybrid functionals, because they represent a mixture between Hartree-Fock and DFT models. Now we will give some examples for hybrid functionals. The *Half-and-Half* method uses the exchange and correlation in the same ratio:

$$E_{xc}^{H+H} = \frac{1}{2}E_x^{exact} + \frac{1}{2}(E_x^{LDA} + E_c^{LDA}) \quad (15)$$

The correlation functional of the LYP functional is not the sum of a local part from the homogeneous electron gas plus a gradient correction which can be written

$$E_c^{LYP} = E_c^{LDA} + (E_c^{LYP} - E_c^{LDA}) \quad (16)$$

and treats the first term as the *local part* of LYP, and the second one as its *gradient correction*.

Mixing additional gradient improved terms *Becke* developed the B3 functional [55]:

$$E_{xc}^{B3} = (1 - a)E_x^{LDA} + aE_x^{exact} + b\Delta E_X^{B88} + E_c^{LDA} + c\Delta E_c^{GGA} \quad (17)$$

The parameters a, b and c are fitted on a test set of molecules. Experiments of additional parameters did not improve the functional [56].

The *BLYP* functional consists of an exchange functional of Becke and the correlation part consist of the spin density with the gradient. This functional was created by Lee Yang and Parr [58]. In the hybrid functionals the exchange correlation energy is calculated using the spin density and the Kohn Sham orbitals while only part of the exact exchange energy is used in this expression. The parameters are fitted to experimental data. One of the most important used functional in the application of the DFT method on transition metal complexes is the B3LYP functional [58–60]. This functional comprises the following expression of different functionals fitted to experimental data:

$$E_{xc}^{B3LYP} = aE_x^{loc} + (1 - a)E_x^{exact} + bE_x^{GGA} + E_c^{loc} + cE_c^{GGA} \quad (18)$$

E_x^{loc} is the exchange energy in LDA, and E_c^{loc} the correlation functional of LDA, E_x^{GGA} is the generalised gradient approximation of the exchange integral and E_c^{GGA} the generalised gradient approximation of the correlation functional. E_x^{exact} is the exact exchange energy. This three-parameter formula assumes that the correlation functional is the sum of a local part of the homogeneous electron gas plus a gradient correction. In particular the B3LYP functional was very popular. This amazing success was fuelled by the surprisingly good performance B3LYP and related functionals demonstrated in many chemical applications, including difficult areas such as open-shell transition-metal chemistry.

2.2.3 Calculation of the Coloumb term

This section account the computation of the classical electrostatic contribution to the electron-electron repulsion. The Potential V_H can be calculated through

$$V_H(r_1) = \int \rho(\vec{r}_2) \frac{1}{r_{12}} d\vec{r}_2. \quad (19)$$

In regular wave function based methods V_H is determined by four-center-two-electron integrals. The problem inherent to this scheme is the large computational load resulting from the number of integrals. We expand the density $\rho(\vec{r}_2)$ in terms of an atom-centered auxiliary basis set α , according to

$$\rho(\vec{r}) \approx \sum c_i \alpha_i(\vec{r}) = \tilde{\rho}(\vec{r}) \quad (20)$$

where tilde indicates that we are dealing with an approximate density (since in practice the auxiliary basis set will never be complete). $\tilde{\rho}(\vec{r})$ is the *Fitted Density*. If we use this approximation, the computational cost for evaluating

E_H is now formally reduced from L^4 to KL^2 . The following equation needs to be solved:

$$\langle \mu | V_H | \nu \rangle = \quad (21)$$

$$\int \mu(\vec{r}_1) \nu(\vec{r}_1) V_H(\vec{r}_1) = \quad (22)$$

$$\int \mu(\vec{r}_1) \nu(\vec{r}_1) \frac{1}{r_{12}} \rho(\vec{r}_2) d\vec{r}_1 d\vec{r}_2 \approx \quad (23)$$

$$\int \mu(\vec{r}_1) \nu(\vec{r}_1) \frac{1}{r_{12}} \tilde{\rho}(\vec{r}_2) d\vec{r}_2 = \quad (24)$$

$$\int \mu(\vec{r}_1) \nu(\vec{r}_1) \frac{1}{r_{12}} \sum c_i \alpha_i(\vec{r}_2) d\vec{r}_2 \quad (25)$$

This method is called 'resolution of the identity' (RI) or *density fitting* in *TURBOMOLE* [51, 60] and reduces calculation time. RI can be not only be used for pure density functionals like BP86, but also for hybrid functionals. The question arises how profitable RI for hybrid functionals is, but in fact the effective scaling of the exact exchange can be reduced from L^4 to L due to the exponential decrease of the density matrix with the center distances in case of large molecules.

2.2.4 Accuracy of the DFT method

Theoretical investigations on inorganic and metal-organic systems were dependent on empirical methods for a long time. Also the huge error in the Hartree-Fock theory due to the missing correlation energy, renders this method useless for such systems. With the availability of density functional theory (DFT) the number of publications which address mechanistic questions has steadily increased. A huge problem of DFT is still not solved: No functional is able to calculate the kinetic energy out of the electron density. The introduction of the Kohn-Sham orbitals is very successful but does not

able the calculation of the accurate kinetic energy. It is still a huge challenge to find an exact functional of the exchange-correlation energy without including the hope on error canceling between exchange and correlation. Despite of the weakness indicated in this method it has been fully accepted in the application on transition metal complexes. The biggest failure of the actual DFT is the missing possibility to enhance systematically the problem introduced by a bad combination of functional and basis set. Systematic errors of the method are the overestimation of the relative stabilities between *high-spin* and *low-spin* complexes and the unbalanced characterisation of relative stability of systems. Necessary at this point is a calibration of the functional and basis set. DFT methods generally benefit from error canceling. All difficult terms are addressed to the exchange-correlation functional whose exact form is still unknown. Fortunately all remaining terms are of the same magnitude but opposite sign, leading to error canceling.

2.2.5 Which exchange-correlation functional should be chosen?

The choice of which functional gives the best result in DFT-calculations is very difficult. There have been a lot of comparison calculations for different molecules on experimental data and on *ab initio* calculations. Usually benchmarking has to be done to find the best combination of functional and basis set. References can be *ab initio* calculations or high accuracy energy models like CBS-Q [61, 62] or CCSD(T). The following examples taken from literature all show better results in energy comparison using the B3LYP functional than the BP86 functional. We focus our investigations on energy comparisons of different pathways employing the B3LYP functional. Different exchange correlation functionals exist and the decision for the most accurate one for the study of transition metal complexes is difficult. In the litera-

ture are a lot of comparative studies are presented with different exchange hybrid functionals. We distinguish these studies between the geometry and energy comparison of DFT results towards *ab initio* calculations. *Barone* [63] validated self-consistent hybrid approaches for the study of transition metal complexes, specifically NiCO and CuCO. He accurately described accurately results for the B3LYP functional compared to the BP functional. Geometrical parameters and binding energies in the majority of cases have been compared to CCSD(T) calculations. *Bauschlicher* [64] presented a comparison of the accuracy of different functionals. A summary of the average absolute and maximum error of different functionals for the G2-molecules calculated atomisation energies was presented. It was shown that more often than not the B3LYP functional showed the smallest error compared to BP86b, BLYP and BP. (Transition metal complexes were not included in these tests). Current comparisons of *Ahlrichs, Furche and Grimme* [65] also compared the recently proposed B97GGA-1 density functional of *Cohen and Handy* [66] that does not compare well against BP86 in cases of Cu_2 and $Ni(CO)_4$ transition metal complex atomisation energies. The additive bond lengths and angles comparisons do not give improved data for $Ni(CO)_4$, $FeCp_2$ and $Mn(CO)_{10}$ transition metal complexes.

The basis set dependence of the DFT results is in some cases very large. Due to the improper 6-31G and 6-311G type basis sets of the Gaussian developer improved basis sets with adaptive constructions are only improved by diffuse and polarisation functions, thus we decided to use the TZVP basis set of *Ahlrichs* as the optimal choice in combination with the B3LYP functional.

2.3 Characterisations of chemical reactions

Chemical reactions can be characterise by stationary points of the *Potential Energy Surface* (PES). These stationary points can be located by the gradient g , the first derivation of the energy E with respect of all coordinates x_i , of the value zero:

$$\frac{\partial E}{\partial x_i} = 0 \quad (26)$$

By means of the second derivation of the energy, these stationary points can be classified. The matrix, calculated from the second derivation of the energy with respect of all coordinates, is called the Hessian matrix H :

$$H_{ij} = \frac{\partial^2 E}{\partial x_i \partial x_j} \quad (27)$$

In case of purely positive eigenvalue of this Hessian matrix, the stationary point can be characterised as a minimum. It is frequently experimentally possible to detect such minima. The other kind of stationary points which are in chemical interest are transition states or saddle points of first order. In such a case one eigenvalue of the Hessian matrix is negative.

In most reactions, knowledge of the transition state and intermediates are necessary for the interpretation of the results. This can then be used for the design of new experiments which push the reaction in a required direction.

In the following section are the most important methods are described which are used for the location of stationary points. All this methods are based on the knowledge of the first derivation. These gradient values can be calculated with numerical accuracy. Due to this fact the prediction of the definite value of a minimum can be never expected. These points have to be accepted as stationary points, which confirm to certain *cut off* values.

2.3.1 Geometry optimisation

In line with the Born-Oppenheimer approximation the electric wave function is independent from the atomic nuclei positions. The intrinsic energy of a non linear molecule with N atoms is a function of $3N-6$ atomic nuclei coordinates which has to be optimised.

2.3.2 Steepest Descent

The simplest algorithm to minimise functional characteristics of a multidimensional function, is the *Steepest Descent* (SD) method.

The gradient of the function has first to be calculated at a certain point. That gradient is orientated to the steepest ascent. The search takes place exactly in the opposite direction to the extent that the functional characteristic is again increasing. The interpolation of the last point gives an approximate minima of the potential energy surface in search direction. Now the gradient has to be obtained again and the search step repeated.

The advantage of this SD-method is the convenience and rapidness. Often the SD-algorithm is used in the case of large gradients at the starting point and then the more improved method used for the search.

2.3.3 Newton-Raphson

For this method an addition to the gradient of the Hessian matrix is required. The function can be then expand by a Taylor serial around this point in case of a accurate saddle point:

$$E(x) = E(x_0) + g(x_0)(x - x_0) + \frac{1}{2}H(x_0)(x - x_0)^2 + \dots \quad (28)$$

This Taylor expansion is aborted after the second order due to the huge cost in the calculation of larger derivations. Due to the expectation that the gradient for the stationary point should be zero, the algorithm is expanded in the next step to:

$$(x - x_0) = -\frac{g}{H} \quad (29)$$

The algorithm for the multidimensional Newton-Raphson method is defined as:

$$E(x) = E(x_0) + g(x_0)(x - x_0) + \frac{1}{2}(x - x_0)H(x_0) * (x - x_0) \quad (30)$$

In this case the inverse hessian matrix has to be multiplied with the gradient vector:

$$(x - x_0) = -(H(x_0))^{-1}g(x_0) \quad (31)$$

The Newton-Raphson algorithm does not necessarily bring us to the minimum. It converges to the next stationary point also if this is a saddle point of first order.

Resulting from eq. 29 the eigenvalues of the Hessian matrix determine the step size. In the case of a eigenvalue close to zero, the step size becomes very large which is not practical. Other methods do exist, which reduces the step size of the Newton-Raphson value to a useful value.

Another problem of this algorithm is the calculation of the Hessian matrix. Such calculation have a larger computational effort than the calculations of

gradients. The improved method used a first approximated Hessian matrix using heuristic values updated in following steps. This method is called the Pseudo-Newton-Raphson method [67–69].

The advantage of this method is the faster convergence compared to the Steepest Descent method. The convergence of a method depends strongly of the elected first Hessian matrix and how the new Hessian matrix is calculated. A very popular method in quantum chemical program packages is the Berny algorithm [70, 71].

2.4 Transition states

It is important to give the used method a good starting point for a transition state by using chemical intuition.

The simplest possibility, but coming with highest computational effort, is to find a chemical useful approximation for the transition state first. Afterwards a frequency analysis is performed and the transition state is modified until the negative eigenvalue of the Hessian matrix is located along the reaction coordinate. It also exists the possibility to use the *eigenvector Following* method [71, 72] to maximise the energy along the reaction coordinate and concurrently minimise the energy in all other directions. This method possesses considerable computational effort due to the calculation of the Hessian matrix in each step. Given that the approximative transition state geometry is close to the exact one, this method can successfully locate the transition state.

A related method without calculating the Hessian matrix in each step is the classical reaction coordinate method [73, 74]. An internal coordinate (in distance matrix coordinates) is here selected as the reaction coordinate. For

fixed values of this internal coordinate all other coordinates are optimised. The highest point of the calculation based on this method is the transition state. This internal coordinate is arbitrary and not the true reaction coordinate so that the calculated results become difficult to interpret [75].

If the geometry of the starting point for the transition state search is close to the exact one, a subsequent optimisation using the Newton-Raphson method is sufficient. In such a case it is necessary to make arrangements avoiding that the result of the optimisation is not located in a minima or a saddle point of higher order.

All previous described methods only include the information of a local structure of the starting point. All other methods use additional information of adjacent minima which are bonded to the reaction coordinate. An interpolation between the two minima determines a structure for the starting point. In the simplest case the difference vector is used between starting material and product and the point along this vector with the highest energy is wanted. This simple method is called the *Linear Synchronous Transit* (LST) [73]. An update is implemented in the GAUSSIAN program package called the *Quadratic Synchronous Transit* (QST) method [76]. Here instead of the linear environment of starting material to product an arc of a circle is added in between. Following the tangent vector in afferent direction the maximum has to be located. This method does not optimise transition states but can obtain a good approximation for the transition state. Using the *eigenvector following* method in the next steps should locate the exact transition state. There also exists the possibility to declare a start geometry for the transition state in addition to the educt and product geometry (QST3) which facilitate

the independent investigation of different pathways with similar minima.

2.5 Reaction pathways

The previous methods characterise chemical reaction locating stationary points on the potential energy surface. In the case of locating a transition state, it has to be confirmed that this transition state connects the desired minima. Therefore we follow the negative eigenvalue of the Hessian matrix, the reaction coordinate of the transition state. Following this path to the lowest energy giving the minimum which is connected to the located transition state. This *Intrinsic Reaction Coordinate* (IRC) [77] method follows the reaction path in direction of the negative eigenvalue. The distinct points on this path can be obtained in optimisations through small steps along this path. One step P_n is given by:

$$P_n = P_{n-1} - \frac{\vec{g}}{|\vec{g}|} \Delta s \quad (32)$$

The gradient is described by g and the step size by Δs . This IRC approach has been introduced by Fukui et al. [78] who used mass-weighted cartesian coordinates. The consequence of large step sizes is a wrong intrinsic coordinate which is not any more the reaction coordinate. This numerical problem has been solved by Schlegel et al. first for cartesian [79] and then for internal coordinates [80].

The investigation of a specific reaction pathway requires the knowledge of conformational differences between educt and product. The educt and the transition state should have the same conformation in the reaction barrier calculation. Only then an accurate activation energy can be computed. This

minimal conformational change can cost a few kJ/mol in the computed reaction barriers which result in a distorted enantioselectivity.

2.6 Solvation models

Theoretical studies of molecules can be easily performed in the gas phase while most chemical reactions in nature occur in solution. Solvent effects can influence stationary points to a significant extend. The calculation of single solvent molecules can be easily done in contrast to the effect of a huge amount of solvation molecules using quantum chemical methods.

Solvent molecules mainly affect the electrostatic potential of the investigated molecules. Due to this fact it should be possible to simulate solvation effects using continuum models [81] describing the investigated molecules in a dielectricum. These methods use the *Self Consistent Reaction Field* (SCRF) [82] model, describing the solute molecule in a cavity of a homogeneous polarisable medium. The solvent effect is composed of the energy value creating the cavity, the electrostatic interactions and the dispersion through charge induction between the solute and the solvent.

The charge distribution of the molecule in the cavity polarises the surface of the dielectricum, resulting in a shielded charge. The charge density of this shielded charge $\rho(r)$ dependence on the dielectric constant ϵ and the electric field $E(r)$ with the norm vector $n(r)$ of the inside of the cavity:

$$\rho(r) = \frac{(\epsilon - 1)\bar{n}(r)}{E}(r)4\pi\epsilon \quad (33)$$

For the simplest model of the cavity (globe) eq. 33 can be solved analytically. The Onsager-Model excludes the dispersion interaction and does not require any SCF process. The disadvantage of this model is the high dependence of the resulting solvation energies on the cavity radii.

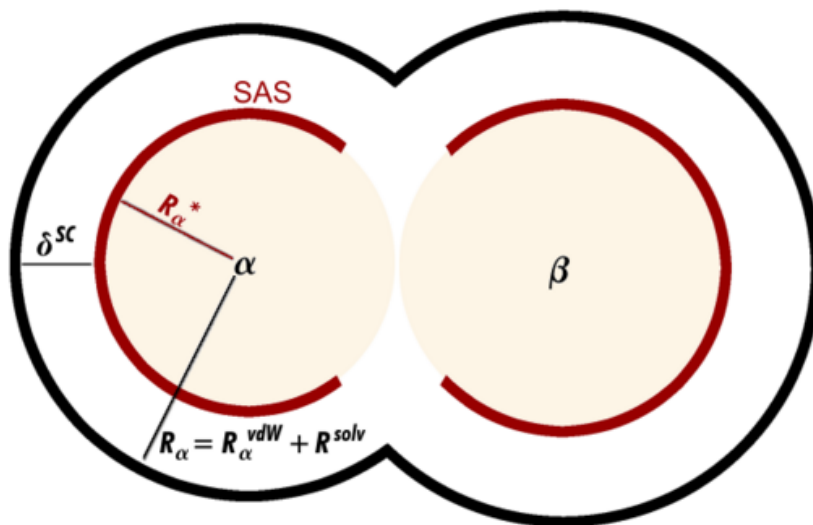


Figure 2: Schematic representation of the Solvent Accessible Surface (SAS)

Better methods fit the surface of the cavity to the *Solvent Accessible Surface* (SAS) of the molecule. The solvent is approximated as a sphere, while the SAS is defined as an envelope of a series of spheres.

There are atom centered spheres with VDW type radii (which are approximately 20% larger than the actual VDW radii), augmented by auxiliary spheres, if necessary, to describe the effective cavity that contains the molecule and that is not accessible to the solvent. Surfaces describing spheres are partitioned, typically into 60 surface triangles, and each triangle is assigned a point charge, the strength of which is adjustable. The electrostatic equations assume, for the moment, a perfect conductor solvent, i.e. a vanishing potential on the cavity surface. This method is used in the *Polarisable Continuum Model* of Tomasi [83] and the *Conductor-like Screening Model* (COSMO) [83–86]. COSMO uses for the calculation of the shield constant an electric

conductor. The potential of the SAS is zero and the shielded constant scaled with a factor dependent of the dielectric constant f :

$$f(\epsilon) = \frac{(\epsilon - 1)}{\epsilon + 0.5} \quad (34)$$

Due to the significant influence of solvent molecules on chemical reaction it is in some case necessary for the reproduction of experimental conditions to include solvents effects. The model describing solvent effects should fit to the molecule surface and include dispersion effects. The accuracy of the method should be than high enough to describe the solvent effects [85].

3 Mechanism

3.1 The investigated reaction pathways

All computations have been performed for the Michael addition of the enamine **3a** (produced from 2,4-pentandione **1a** and (*S*)-alanine dimethyl amide **2a**) to methyl vinyl ketone **4**. Three mechanistic possibilities were investigated (Scheme 4), namely the metal-free *background* reaction of **3a** with **4**, the Michael addition of **7a** a coordinated enamine to the intramolecular coordinated Michael acceptor, and the reaction of the copper-coordinated aza-enolate **9** which is produced upon deprotonation at the enamine nitrogen atom (Scheme 4). In this chapter, the focus lies on the elucidation of the reaction mechanism rather than on the calculation of the enantiomeric excess which will be investigated with different values of amino acids in the next chapter. In all our calculations in this chapter the enone approaches the Michael donor from the *re* side. In the nucleophilic attack of the coordinated enamine and aza-enolate we will also investigate ligand effects: If an enamine is coordinated on copper(II) two coordination sites are free and can be filled with different ligands. In case of the coordinated aza-enolate just one coordination site is free which we will investigate with several ligands. Our goal is to find the reaction path with the lowest barrier. Furthermore we have been proposing an experiment using a secondary enamine which block the copper catalyst and theoretically also the metal-free reaction. A product is in such an experiment not expected if the proposed mechanism is true. In the last section we have been additionally investigated an outside attack of the Michael acceptor in gas phase and with solvent effects using the two continuum models COSMO and PCM.

3.2 Metal-free background reaction

The experiments show that there is indeed a non catalyzed background reaction which proceeds in the absence of any metal salt [39]. This reaction path is not only much slower than if catalyzed by the metal, but also shows lower enantioselectivity (typically, 57-70% ee for enamines derived from valine). According to the performed calculations, the direct addition of **3a** to **4** is a rather unfavorable step at least in the gas phase if one starts from the most stable conformation of **3** in which the hydrogen atom at the enamine nitrogen forms a hydrogen bond to the carbonyl oxygen atom. The reason is, that the addition forms a highly polar, formally zwitterionic structure with a positive formal charge on the enamine nitrogen and a formal negative charge on the oxygen atom of the Michael acceptor. Such a transition state is not locatable in gas phase. Optimisation always drop to the educts. There is a stabilisation of a zwitterionic structure if one puts the system into a dielectric continuum that simulates the influence of an aprotic solvent, making such a reaction attractive with a barrier of 91 kJ/mol. But this studies will be discussed in more detail in chapter 4.5. First we look for an alternate reaction path in gas phase, in which the N-H proton can be transferred to the oxygen atom of the acceptor upon C-C bond formation. The transition state for such a reaction path is shown in Fig. 3. In this figure (and the following ones), the Michael acceptor is marked with a shadow for the convenience of the beholder. Furthermore, a circle highlights the side chain of the amino acid (a methyl group in our calculations) which is the group that triggers the enantioselectivity of the reaction. The computed activation energy is 97 kJ/mol for the transition state **TS 3a/6** (see Fig. 3) which lead to the addition product. This barrier height is consistent with the observation of a slow reaction at ambient temperature. The enantioselectivity (crossing the folded

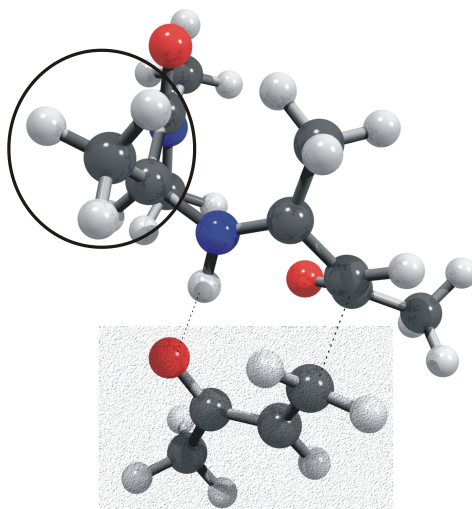


Figure 3: Transition state **TS 3a/6** for C-C bond formation in the metal-free background reaction. Note that proton transfer from N to O occurs simultaneously.

transition state TS3a/6) with a methyl group in the amino acid side chain starting from **3a** and a *tert.*-butyl group in **3b** will be calculated and discussed in chapter 4.5. In this case, the N-H bond is broken during C-C bond formation, and no imminium ion intermediates is performed. This pathway is not possible for secondary enamines which are formed if one starts e.g. from a N-methylated amino acid. Indeed, in an experimental study suggested by the present work, no reactivity has been observed in such a case.[86] We can conclude indeed out of the calculations in gas phase and experiments that the folded transition state Fig. 3 is the most likely one.

3.3 Nucleophilic attack through a coordinated enamine

Although the nucleophilicity of the enamine most likely *decreases* upon coordination to Cu^{2+} , this reaction path (Scheme 4) cannot be excluded from the outset since activation of the Michael acceptor upon coordination to the Lewis acidic metal center has to be expected. The calculations showed that the enamine **3** mainly binds through its carbonyl oxygen atoms to Cu^{2+} while the enamine nitrogen binds, if at all, only loosely. There is also no tendency for the amide nitrogen at the C-terminus of the amino acid to coordinate. A neutral water molecule and Michael acceptor **4** completes the coordination sphere of the copper ion in our model system **7a**. The transition state **TS7a/8a** of the following step of C-C bond formation is shown in Fig. 4. The computed activation energy is 94 kJ/mol and thus of the same magnitude as for the background reaction. The structure of the reactive species **7a** in case of the coordinated enamine was not clear from the beginning. We have been locating the transition state **TS7a/8a** first and then performed an IRC (intrinsic reaction coordinate) calculation across the reaction coordinate to optimise the educt.

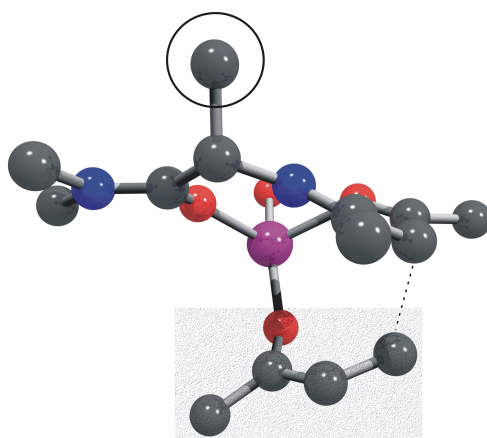
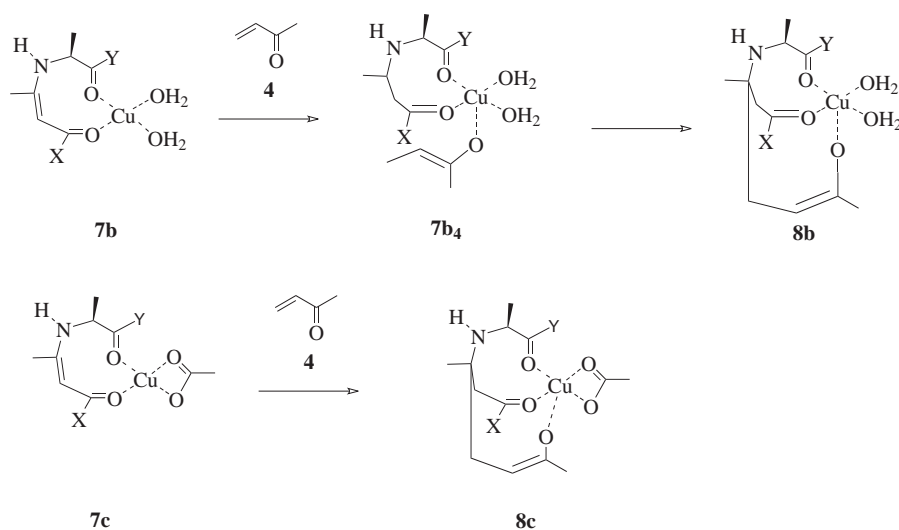


Figure 4: Optimised transition state **TS7a/8a** of a coordinated enamine on copper (II).



Scheme 5: Investigated pathways for C-C bond formation of a coordinated enamine on copper(II) and methylvinylketone.

The reactive species consisting of a coordinated enamine needs two additional ligand to get a full occupied coordination sphere. First the Michael acceptor and a water molecule has been added (**7a**). Two different ligand

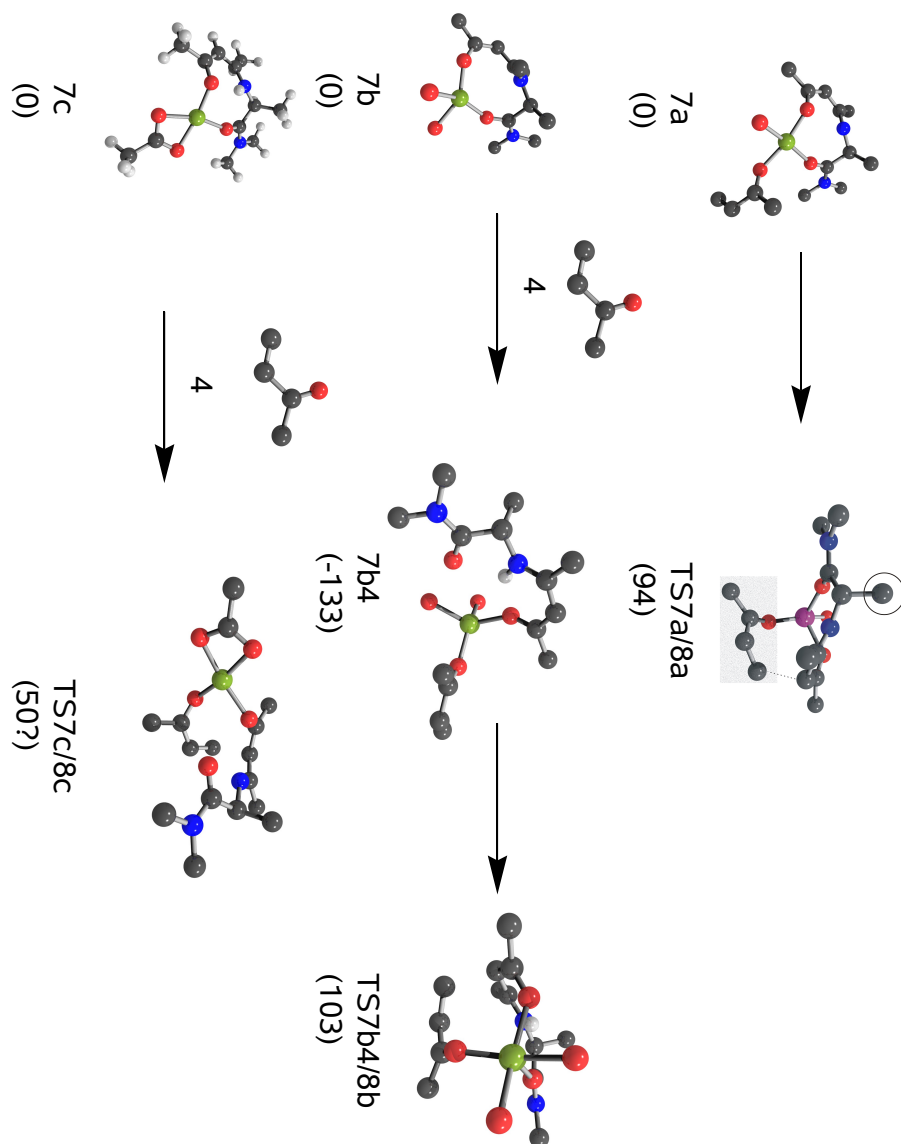


Figure 5: Optimised structures investigated in different reaction pathways of the coordinated enamine on copper. Number in brackets show the relative energies in kJ/mol. Note that **TS7c/8c** doesn't lead to the desired product.

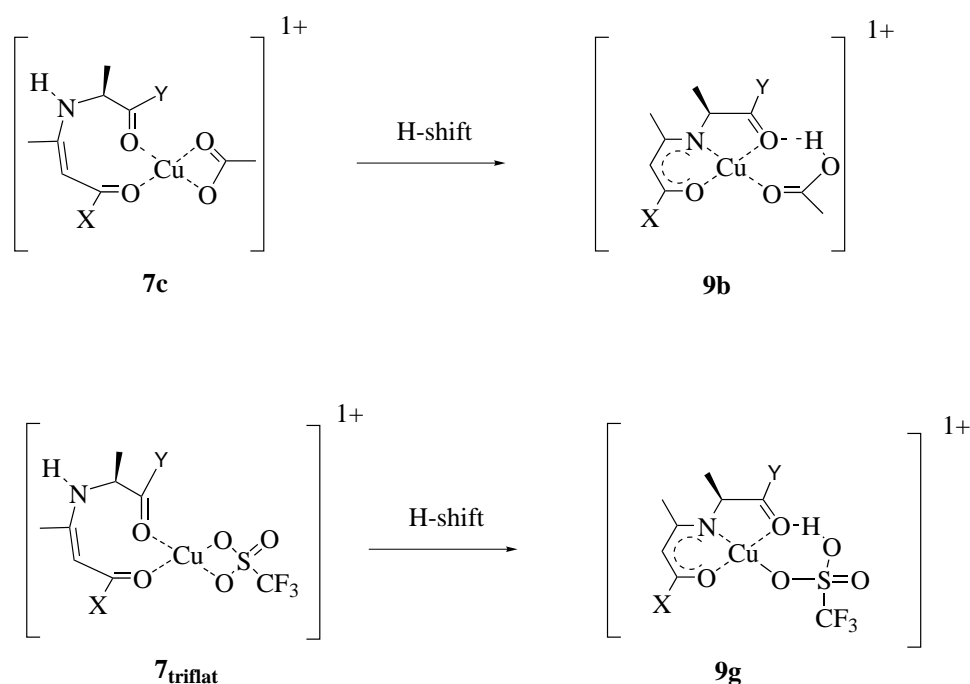
combinations have been additionally investigated (Figure 5). In molecule **7b** the coordination sphere around copper contains two water molecules. Before C-C bond formation an axial binding of the Michael acceptor oxygen to the copper center (**7b₄**) takes place. The C-C bond formation passes intramolecularly through transition state **TS7b₄/8b** (Fig. 5). The second possibility is a coordinated acetate ligand on two sites to copper in the coordination sphere (**7c**). The calculation of the direct reaction barrier **TS7b/8b** without a previous coordination of the Michael acceptor on copper gives a small reaction barrier of 30 kJ/mol. Reason is the described huge binding energy of the Michael acceptor **4** to the reactive species **7b** computed in 133 kJ/mol due to the doubly charged complex resulting in **7b₄**. The C-C bond formation reaction barrier has been computed with 103 kJ/mol giving transition state **TS7b₄/8b**. Cu(OAc)₂ is the best catalyst in the experiments. Due to this fact an acetate molecule has been used as the additional ligand (**7c**). Transition state **TS7c/8c** has been optimised and shows an unexpected geometry due to a different mechanism with similarity to the background reaction. The reaction barrier of the C-C bond formation with 50 kJ/mol shows a different reaction path not comparable with the main mechanism. The reaction barriers of C-C bond formation of a coordinated enamine are in the same value as the metal free background reaction and can be excluded.

3.4 Nucleophilic attack through a coordinated aza-enolate

In case of the Fe(III) catalyzed Michael addition of β -diketones, the acidity of the latter is increased so much upon coordination to Fe³⁺ that it protonates the surrounding molecules and thus becomes a coordinated enolate. If the Cu(II) catalyzed reaction of the enamine derivative proceeds in an

analogous way, this would require a deprotonation at the enamine nitrogen. Our calculations show that upon removal of this proton, the nitrogen atom forms a strong dative bond to the copper center. As a consequence, the rigidity of the nearly square planar complex **9** is enhanced. We performed first the calculations both with a water and with an acetic acid molecule (coordinated through its carbonyl oxygen, see below) occupying the fourth coordination site. These molecules were chosen to mimic any of the weak oxygen donors present in the reaction mixture. Originally it was assumed [87] that the enamine coordinates as a tridentate ligand to the face of an octahedral coordination geometry around the copper center. According to our calculations, such an intermediate deserves no further consideration. Scheme 4 presents (right side) the investigated reaction pathways of a coordinated aza-enolate on copper with a methylvinylketone. It is not surprising that the deprotonation significantly increases the nucleophilicity of the complex. The activation energies for the C-C bond forming step of the reaction are greatly reduced, from 94 kJ/mol for the coordinated neutral enamine to 77 kJ/mol for a coordinated aza-enolate if water is used as a co-ligand (**9a**). If the water molecule is replaced by acetic acid (**9b**), the activation energy (including ZPVE) is further reduced a bit (to 70 kJ/mol) but stays in the same ballpark. The transition state **TS 9b/10b** for this latter case is shown in Fig. 6. It can be seen that the amino acid side chain (a methyl group in our model system) adopts an angular position with respect to the coordination plane. Although we will not yet discuss the calculated enantiomeric preference for this step (This will be described in detail in chapter 4), Fig. 6 suggests that an attack of the methyl vinyl ketone **4** from above will require a distortion of the coordination geometry that leads to a higher activation energy. This investigation of different sizes of the amino acids used as the chiral ligands

will be described in chapter 4. The question naturally arises, whether coordination to Cu^{2+} increases the acidity of the enamine such that a coordinated aza-enolate exists in sufficient concentration in the reaction mixture. Gas phase calculations show a reduction of the proton affinity from 1538 kJ/mol for the free aza-enolate down to 606 kJ/mol for the square planar complex **9a** in case of a coordinated water molecule which is easily understood by electrostatic arguments. The proton affinity of the surrounding molecules is significantly higher (methyl vinyl ketone **4**: 858 kJ/mol; typical solvent molecules such as acetone: 844 kJ/mol). At first sight, these numbers suggest that a coordinated enamine is acidic enough to lose its proton to the reaction mixture. One should however be careful since the comparison of gas-phase proton affinities is not enough to calculate acid/base equilibria in solution. Furthermore, the acidity increase is weaker than in the case of the Fe(III) catalyzed Michael addition of enones, most likely due to the smaller charge of Cu^{2+} compared to Fe^{3+} . Therefore, we also investigated a second possibility for the formation of a coordinated aza-enolate, namely the transfer of a proton to a basic co-ligand such as acetate (Scheme **6**). This reaction is exothermic by 58 kJ/mol in the gas phase, and should remain so in solution, because the solvation energies of **11** and **9b** are probably similar. Upon proton transfer, the bidentate acetate ligand is transformed to (monodentate) acetic acid, the enamine nitrogen taking over the coordination site thus released (Scheme **6**). An analogous calculation with a triflate ligand instead of acetate shows a much reduced tendency to transfer a proton (in the gas phase this reaction is still exothermic by 28 kJ/mol). This reduction of course reflects the lower basicity of triflate compared to acetate.



Scheme 6: Investigated pathways for intramolecular proton shifts in feasible complexes.

3.4.1 Ligand effects in the C-C bond formation of a coordinated aza-enolate on copper(II)

In the central reaction pathway of the coordinated aza-enolate calculations have been performed for the reaction barriers of C-C bond formation with different ligands (last section presented the results to the ligands water and acetic acid) **L**: Ammonia, ethanol, methanol and acetone in the species **9** (Scheme 2). The lowest reaction barrier with a value of 65 kJ/mol (without ZPVE) crossing transition state **TS9b/10b** has been calculated with the ligand acetic acid, described in the previous section. All other calculated reaction barriers show a higher activation energy up to 75 kJ/mol (for ligand acetone crossing **9f/10f**). The ligand methanol coordinated in the reactive

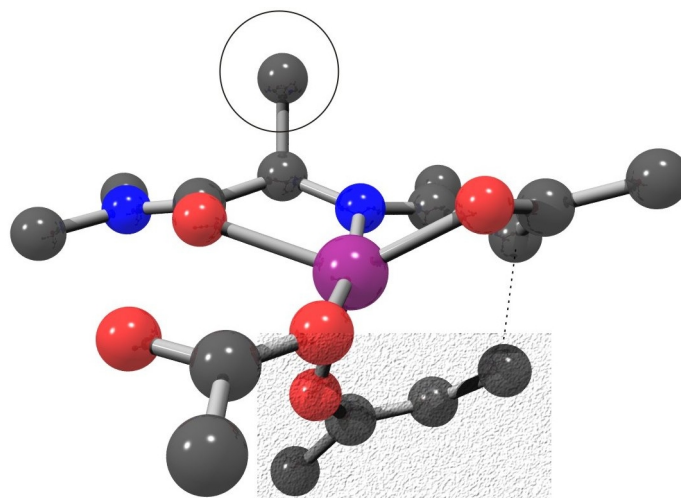


Figure 6: Transition state **TS 9b/10b** for C-C bond formation between a coordinated aza-enolate and the Michael acceptor. An acetic acid molecule serves as co-ligand.

species gives a transition state **TS9d/10d** and a computed barrier of 72 kJ/mol. Also ethanol in **TS9e/10e** and ammonia in **TS9c/10c** with 73 and 69 kJ/mol are barriers computed in the same magnitude. The ligand ammonia brings a smaller reaction barrier resulting from the higher nucleophilic property into the reactive species, but this molecule should be not consist in the experimental reaction mixture. Cause for the low barrier in case of acetic acid is the intramolecular hydrogen bridge between the acetic acid and aza-enolate in species **7b** and transition state **TS9b/10b**. We conclude that the main path of the reaction mechanism is the nucleophilic attack of the coordinated aza-enolate and acetic acid as the co-ligand on the Michael acceptor. All computed reaction barriers are presented in Table 1.

3.5 Experimental proof of the mechanism:

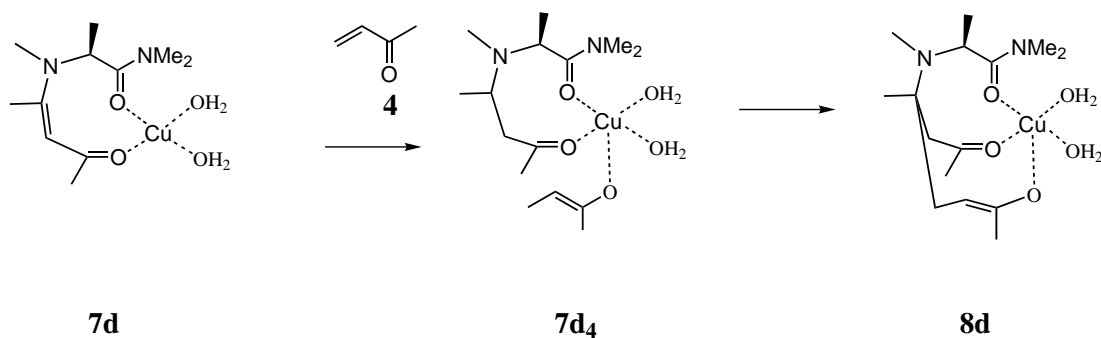
Non-reactivity of a secondary enamine?

The mechanism can be proved by experiments using a secondary enamine in the copper catalyzed reaction (Scheme 7). Due to the missing hydrogen atom at the enamine nitrogen the intramolecular proton shift to the basic co-ligand (Scheme 4) before C-C bond formation is blocked. Our proposed experiment should block this intramolecular hydrogen shift and the catalyst reactivity due to the no existing deprotonation of the enamine. Also the metal-free background reaction should be blocked due to the not existing intramolecular hydrogen shift in the described folded transition state. Our proposed experiment has been performed by *Christoffers et al.* We suggest that if the secondary enamine used in the Michael reaction is non-reactive, our proposed mechanism should be true. From the theoretical point of view we expect that using a secondary enamine lead to a similar huge barrier as described in the previous section 4.3 (C-C bond formation of a coordinated enamine). To prove this we have been first computing the reaction barrier using a secondary enamine (Scheme 7). Our results show a similar geometry of the reactive species like in the case of a coordinated enamine. Similar to the path of a coordinated enamine first the Michael acceptor axial binds to copper(II) in species **7d** with 106 kJ/mol (leading to the species **7d₄** following reaction barrier of 110 kJ/mol in the C-C bond formation. The transition state **TS7d₄/8d** is shown in Fig.7. Our suggested experiment have been successfully performed by *J. Christoffers and L. Diedrich*. A secondary enamine has been synthesised and the reactivity in the Michael reaction investigated (Scheme 8). These experiments have been performed for the catalyzed reaction. There has been observed a non-reactivity of the secondary enamine. This experiment confirms our calculation for the pro-

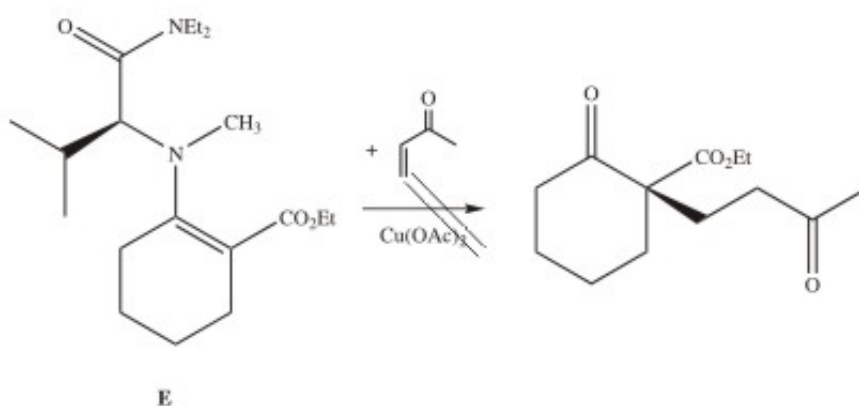
3.5 Experimental proof of the mechanism:
Non-reactivity of a secondary enamine?

Mechanism

posed mechanism. Using a secondary enamine the deprotonation and leading to a coordinated aza-enolate is blocked. Due to the high reaction barrier of a Michael reaction with a secondary enamine which has been calculated this pathway is blocked. Also the non-reactivity in the metal-free background reaction of the secondary enamine shows that the intramolecular hydrogen bond exist in the folded transition state. Our proposed mechanism including the nucleophilic attack of a coordinated aza-enolate on copper(II) is indeed now proved by experiments.



Scheme 7: Investigated reaction pathway for C-C bond formation between a secondary enamine and methylvinylketone in the computed system.



Scheme 8: Experimental investigated reaction of a secondary enamine in the Michael reaction.

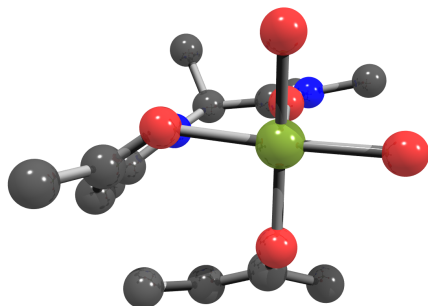


Figure 7: Optimised transition state **TS7d₄/8d** for C-C bond formation of the secondary enamine coordinated on copper(II) (Here displayed in green) with two water co-ligands.

3.6 Kinetics and Electro Spray Ionisation (ESI) mass spectroscopy

We suggested experiments to study kinetics of this reaction. In our proposed mechanism occurs on one copper site. The performed experiments of *Christoffers et al* show that there exist a linear dependence of the relative kinetic constant on the catalyst concentration (Fig. 8). This confirm that the reaction mechanism occurs at one copper center. In the opposite situation of more than one copper centers in the reaction mechanism would effect in a non linear dependence.

Electro Spray Ionisation mass spectroscopy has been performed [88] with a reaction mixture (see Fig. 12): Enamine **A** and Catalyst **B** ($\text{Cu}(\text{OAc})_2$) in a ratio of 1:1 using the solvent acetone. Fig. 9 gives the measures spectrum. Such a high concentration of catalyst was necessary to enable the measuring of interesting copper complexes. Signals of such complexes have not been observed using reaction conditions (catalyst concentration of 1 %). The

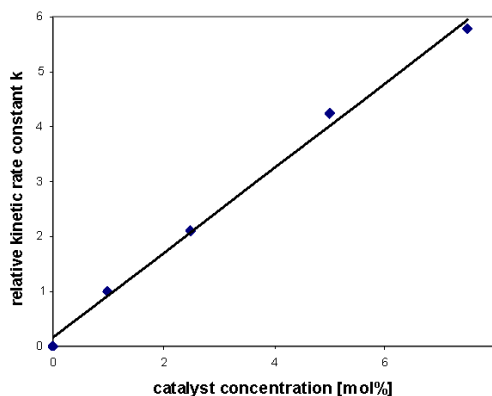


Figure 8: Result of the kinetics experiments showing the dependence of the relative kinetic constant on the catalyst concentration. Data: 6-ring-enamine 500mg (1,54 mmol) (0,154 mol/l), methylvinylketone 189 mg (2,70 mmol, 1,75 eq.), $\text{Cu}(\text{OAc})_2 \cdot \text{H}_2\text{O}$ 0-7,5 mol, acetone 10 ml with 0,01 mol/l octanol as the reference.

most interesting measured signal in the ESI spectrum (Fig. 10) is at 444 amu (coordinated aza-enolate and acetone as the co-ligand on copper(II)) with the typical copper isotope pattern (69 % Cu^{63} / 31 % Cu^{65} : **C** in Fig. 12). This molecule shows fragments into a species of the coordinated aza-enolate **D** (Fig. 11 (at 386 amu with the copper isotope pattern) and acetone (58 amu). This spectrum proves that the reactive species in the mechanism indeed consists of a coordinated aza-enolate and acetone as the co-ligand due to the used solvent acetone. In the previous section we proposed acetic acid as the co-ligand, but this would be the case in gas phase. It is clear that acetone as the solvent causes a fast ligand exchange of acetic acid and an acetone molecule. A signal of species **7c** and **9a**, respectively can not be observed in the spectrum. The question appear if there exist any other complex with the same mass 444 amu. But we can exclude that the observed signal of

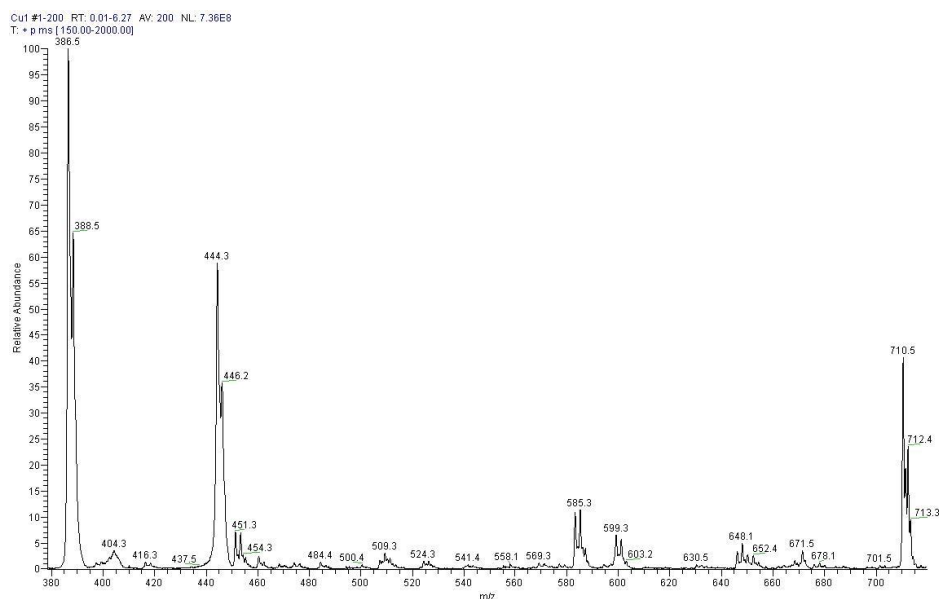


Figure 9: ESI spectrum of the investigated system. Ratio between catalyst $\text{Cu}(\text{OAc})_2$ and enamine is 1:1 in the reaction mixture.

444 amu belongs to a complex of a coordinated enamine on copper. In this case the co-ligand acetone would be deprotonated what we can exclude. We conclude that the enamine nitrogen gets deprotonated. The acetic acid molecule is evidently slight bounded and gets substituted through acetone either in solvent or in the ESI process.

3.7 Solvent effects

In a polarisable continuum model, Solvation energies increase with the dielectric constant of the solvent and the polarity of the solute. Additionally, the surface energy of the cavity that is formed in the solvent to accommodate the solute as well as van der Waals typed interaction between the solute and the solvent are taken into account.

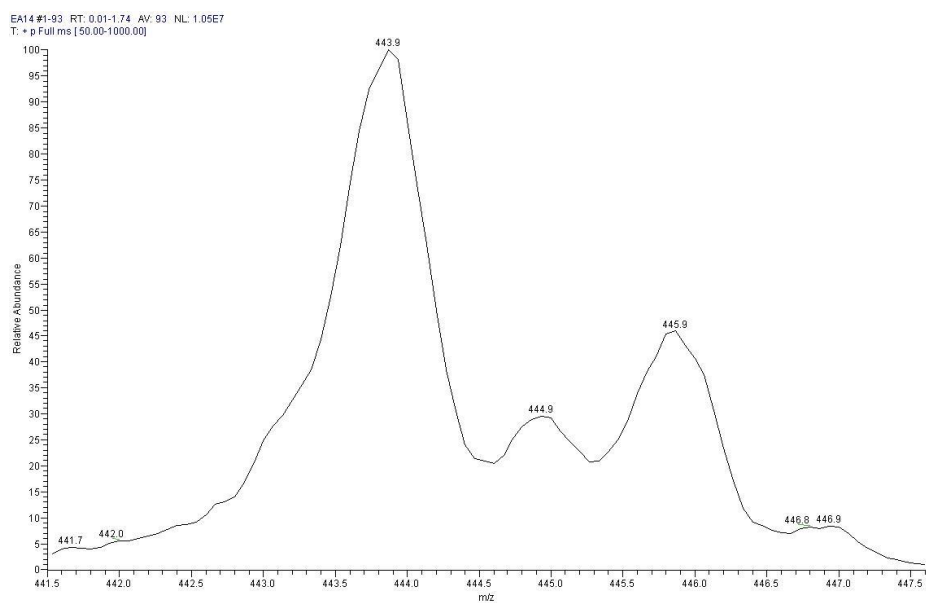


Figure 10: ESI spectrum of the fragment at 444 amu (C).

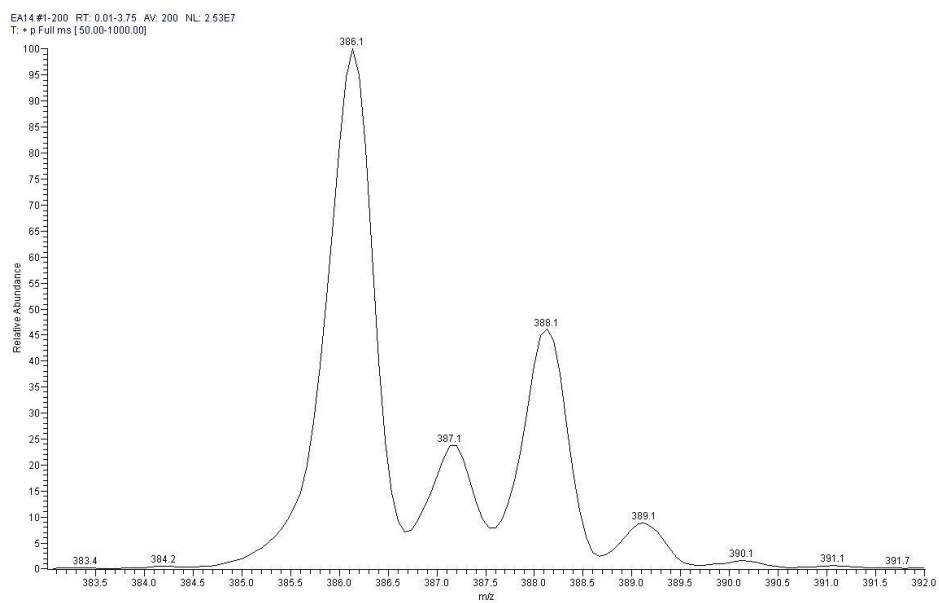


Figure 11: ESI spectrum of the fragment at 386 amu (D).

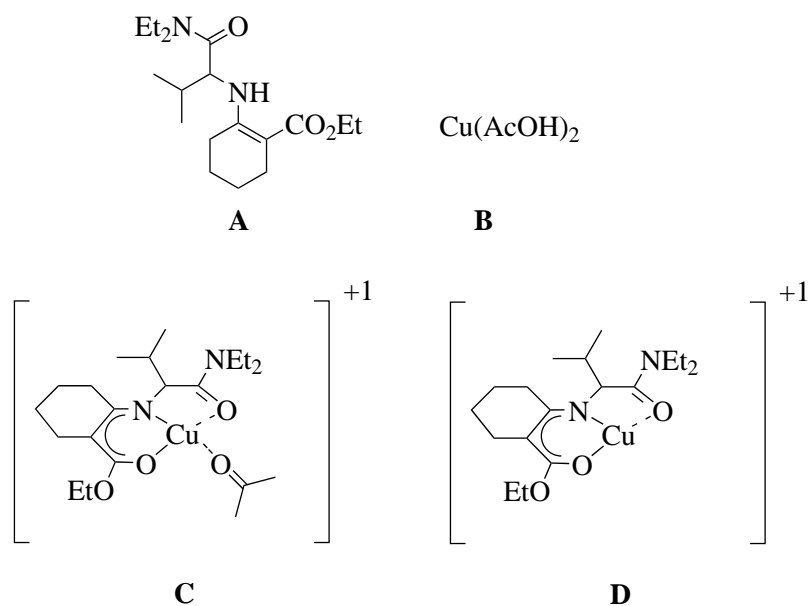


Figure 12: Investigated system in mass spectroscopy (ESI).

All previously described calculations on the mechanism in the copper(II) catalyzed Michael reaction were performed in gas phase. The experiments have been performed in solution, mostly acetone and dichloromethane. We concentrate now on solvation effects on the mechanism using PCM and COSMO, two models for the simulation of solvent effects (section 2.6). We focus in this section first on the calculations of solvation energy of the reactive species **9a** and following two possible transition states for C-C bond formation. There could be an *outside* attack on the Michael acceptor or an *inside*. In the *inside* attack the carbonyl oxygen atom of the Michael acceptor **4** coordinates to copper upon C-C bond formation, and in the *outside* attack is the steric interaction between **4** and **9a** much smaller. However a large dipole moment is formed upon *outside* attack and the solvent accessible surface is also large. We can therefore expect that the *outside attack* becomes more attractive in

polar solvents. We have been investigating solvent effects in these two different paths optimising the transition states first in gas phase and with solvent effects. We conclude from the first calculations in gas phase that a high polar transition state by an outside attack (Fig. 13) of the Michael acceptor with a reaction barrier of 119 kJ/mol is much less preferred than an inside attack with a computed barrier of 71 kJ/mol in gas phase. The optimised transition state for the outside attack **TS-outside** is shown in Fig. 13. The solvation energy is for the isolated reactive species **9a** and the Michael acceptor **4** much higher than for the transition states. All structures are stabilised in solution, but the value of this stabilisation is different. The pathway of the outside attack of the Michael acceptor has in acetone a reaction barrier of 124 kJ/mol and the inside attack 101 kJ/mol. We conclude that all reaction pathways have a higher barrier but this value of stabilisation depends on the geometry and dipole moment in the transition state. The difference between the pathways of in and outside attack is in the gas phase 48 kJ/mol and in the solvent acetone 23 kJ/mol. The solvation energy in acetone for the outside attack of the Michael acceptor is not huge enough to be prefer to the outside attack. Two different continuum models PCM and COSMO has been used for this studies. The differences between these methods are quite small. We have been observing difficulties in the optimisations of minima and transition states using PCM and COSMO. The convergence of this optimisations show an unevenness of the energy potential surface. Also we have been observing additional small negative frequencies in optimised minima and transition states using continuum models. Table 2 consist of the computed reaction barriers for the insides and outside attack in gas phase and in solvent using the PCM and COSMO method. The favoured reaction path found in gas phase calculations remain-preferred also in acetone. Calcula-

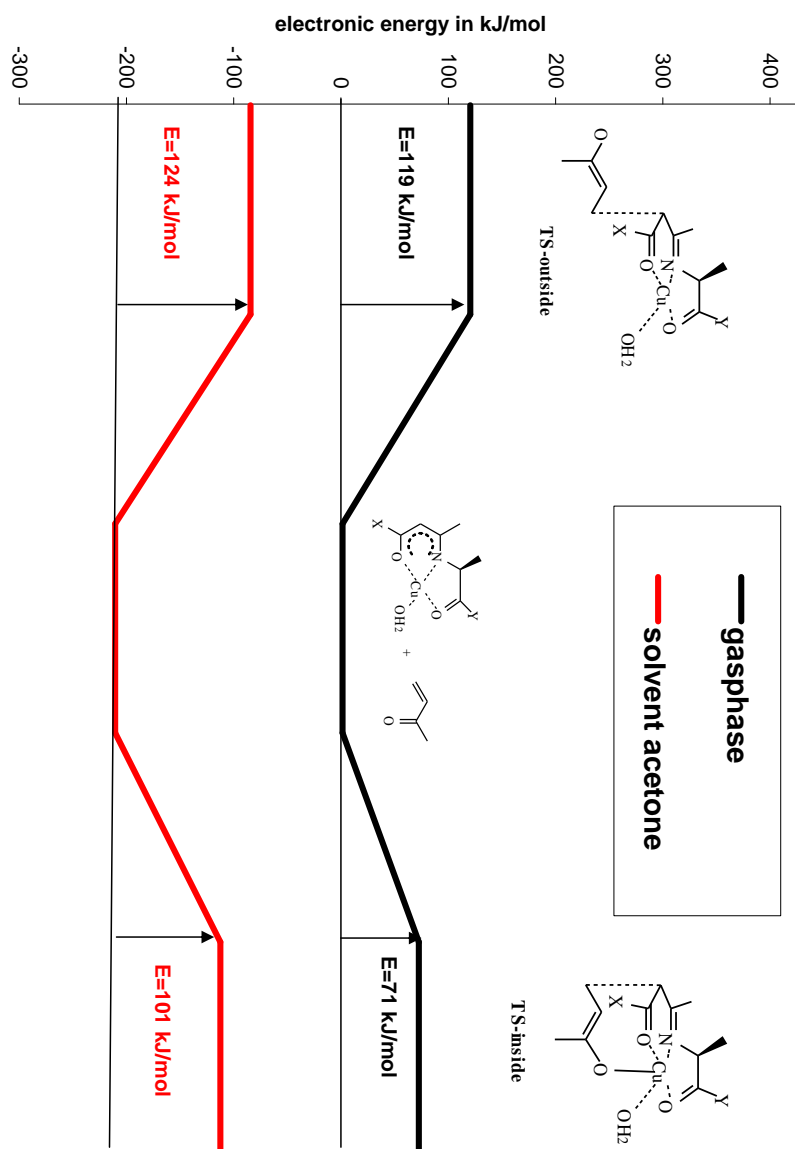
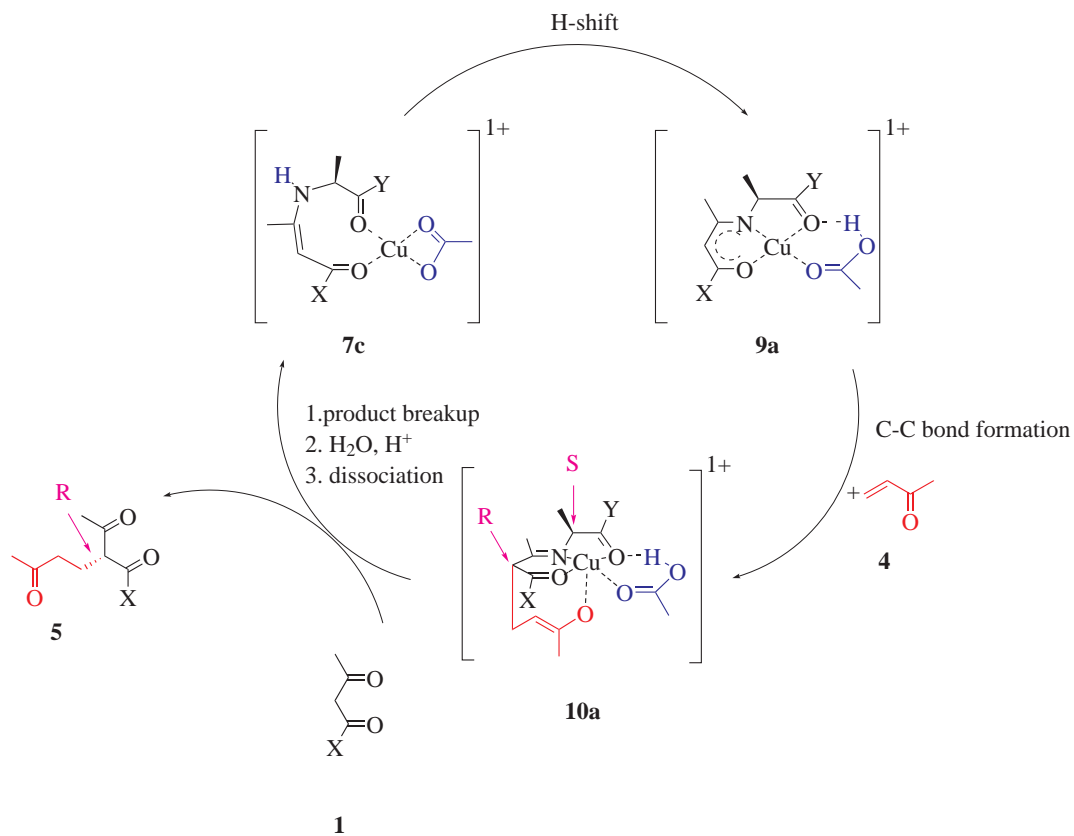


Figure 14: Diagram of the calculated reaction barriers of inside attack and outside attack (study in gas phase and including solvent effects).

reaction channel with a barrier that is reduced by ~ 25 kJ/mol. This reaction channel not only supports a reasonably fast reaction at ambient temperature, but most likely also leads to the highest enantioselectivity because of the rigid transition state with the angular amino acid side chain. Based on this calculations, we proposed the catalytic cycle presented in Scheme **9**. The energy profile for all investigated pathways is presented in Fig. 15. In all cases, the N-H bond is broken either before or during C-C bond formation, and no imminium ion intermediates are performed. These pathways are not possible for secondary enamines which are formed if one starts e.g. from a N-methylated amino acid. Indeed, in an experimental study suggested by the present work, no reactivity has been observed in such a case, either for the metal-free background reaction or in the presence of $\text{Cu}(\text{OAc})_2$.



Scheme 9: Computed catalytic cycle for the copper catalyzed Michael reaction.

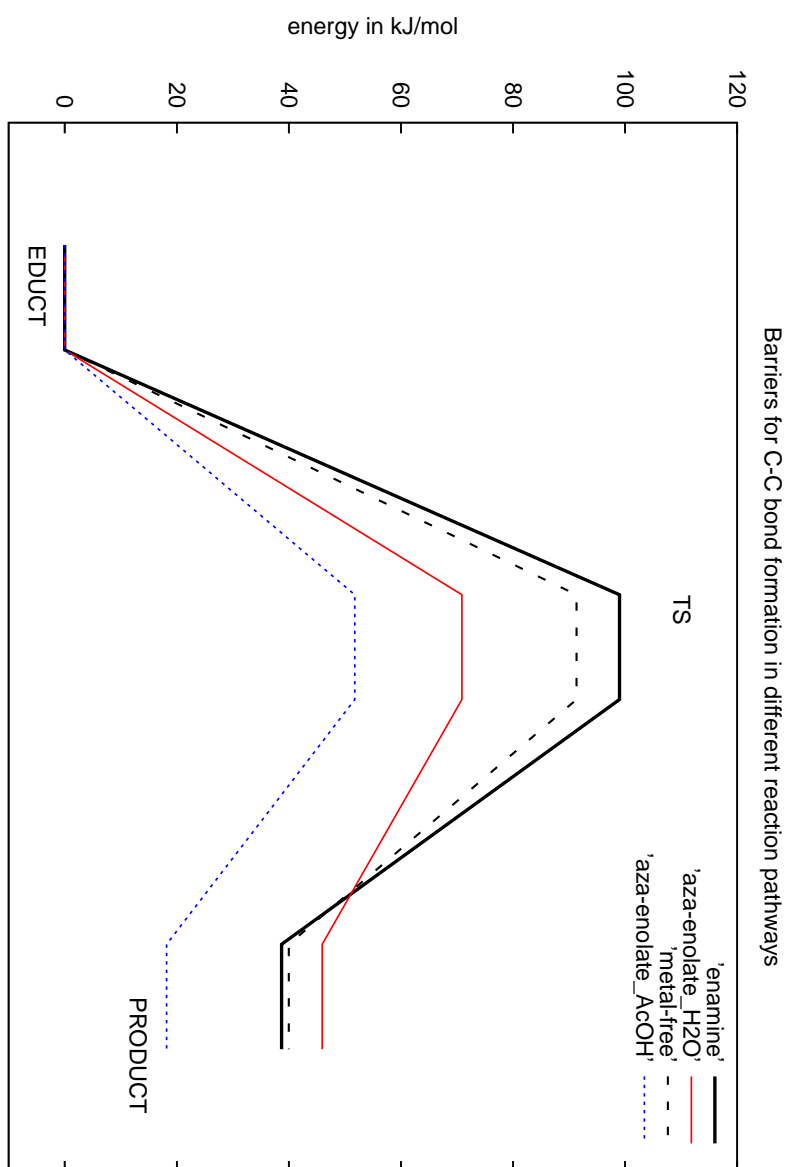


Figure 15: Energy profile of all investigated reaction pathways of the Michael addition mechanism. Note that these barriers include electronic energy without ZPVE.

4 Enantioselectivity

4.1 Calculation of enantioselectivity

In this section we explore these pathways for chiral auxiliaries [32, 39, 43] with side chains of different sizes, namely for intermediates (aza-enolates) derived from L-alanine (with a methyl group side chain), L-valine (isopropyl) [38], L-*tert.*-leucine (*tert.* butyl) and L-neopentylglycine (neopentyl) [89]. We use the same model system as in [90], namely an enamine derived from pentone-2,4-dione and the amino acid (protected as a dimethylamide at the carboxyl group), which is deprotonated and binds to three sites of a square planar coordinated Cu^{2+} , compounds **9a,h-j** and to which methylvinyl ketone **4** is added, approaching the Cu center either from the less hindered side to form products **10a,h-j** through the *matched* transition state **TS9/10a,h-j**, or through the *mismatched* transition state **TS9/11a,h-j** from the hindered side giving products **11a,h-j** with the opposite configuration at the newly formed stereo center. These products are diastereomers (not enantiomers) as long as the chiral amino acid is still bound to the substrate, but for unsymmetric dicarbonyl compounds these two products after hydrolysis lead to two enantiomeric products. In what follows, the diastereomeric ratio of the C-C coupling step is therefore identified with the enantioselectivity of the overall transformation. Experimentally, varying enantioselectivities have been observed for different solvents. In addition to gas phase calculations, we therefore also performed calculations that include solvent effects through a polarisable continuum model.

4.2 Methods of Computation

Assuming kinetic control, the enantiomeric excess is defined as

$$ee = \frac{k_1 - k_2}{k_1 + k_2} = \frac{\frac{k_1}{k_2} - 1}{\frac{k_1}{k_2} + 1} \quad (35)$$

where k_1 and k_2 are the rate constants for the formation of the major and the minor stereoisomer, respectively. From the Arrhenius ansatz

$$k_i = A_i \exp\left(-\frac{E_A^{(i)}}{RT}\right) \quad (36)$$

we get

$$\frac{k_1}{k_2} = \frac{A_1}{A_2} \exp\left(-\frac{\Delta E_A}{RT}\right). \quad (37)$$

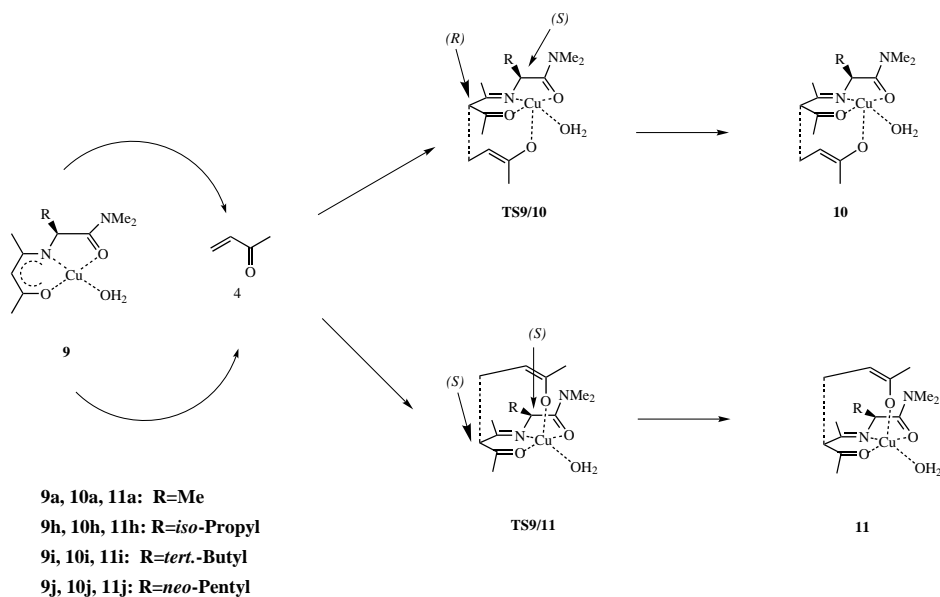
The calculation of the pre-exponential factors A_i for a complex reaction is a formidable task, since this would require the partition function (including information on the whole conformational space) of the system. We therefore ignore $\frac{A_1}{A_2}$ in this study. Measuring the enantioselectivity at different temperatures might provide experimental information on the ratio of the pre-exponential factors. For the difference in the activation energies, ΔE_A we use the total energy difference (without zero-point vibrational energy) between **TS9/10** and **TS9/11**. Note that thermal contributions to the activation enthalpy nearly cancel. The enantiomeric excess is then calculated setting $T=298\text{K}$ in eq. (37). for ambient temperature ($T=298\text{K}$). Total energies were obtained by density functional calculations performed with the Gaussian03 [91] and TURBOMOLE [92, 93] quantum chemical program packages. TZVP basis sets [94] have been used throughout. In all cases the B3LYP exchange correlation functional [55–58] has been used. All stationary points on the potential energy surface (local minima and transition structures) were

characterised by a harmonic vibrational analysis, which was also required to calculate the zero-point vibrational energy which is added to the electronic energy at the stationary points. DFT (B3LYP) calculation to optimise all minima and transition states. Solvent effects have been calculated by the polarisable continuum model COSMO (conductor-like screening model) [84] as implemented in Gaussian03 (keyword CPCM [95, 96]) and TURBOMOLE [92]. To calculate solvent effects, we start from optimised gas-phase geometries and perform a full structure optimisation of the system in the solvent. For the cavity construction we have used the atom radii of *United Atom Topological Model (UA0 parameters set)*. We model solvent effects for acetone which has a dielectric constant $\epsilon = 20.7$ at ambient temperature.

Typical errors for activation energies obtained by density functional calculations are significantly larger than $RT \approx 2.5$ kJ/mole, such that a calculation of the enantioselectivity would be meaningless if these errors were statistical. However, quantum chemical methods usually show quite systematic errors such that some error compensation can be expected in the calculation of ΔE_A if energies of very similar transition structures are compared. As we will see, the transition structures that we compare (**TS9/10** and **TS9/11**) are quite different in nature, so a caveat is in order here. Nevertheless, such calculations may still provide trends and a useful overall picture even if the calculated selectivities are not quantitatively correct. Several theoretical studies concerning the calculation of enantioselectivities have been published recently [97–107].

After the general mechanism of the reaction has been established in the previous sections we now concentrate on the direct calculation of the reaction enantioselectivity in dependence of different sizes of amino acids (Scheme 10). In this section we explore these pathways for chiral auxiliaries with

side chains of different sizes, namely from L-alanine (methyl group), L-valine (isopropyl group), L-*tert.*-leucine (*tert.* butyl group) and L-neopentylglycine (neopentyl). Apart from the amino acid side chains, we use the same model system: Michael donor **9** and Michael acceptor **4**. Compounds **9a,h-j** and which adds to methylvinyl ketone **4** which approaches the Cu center either from the less hindered side to form products **10a,h-j** through the *matched* transition state **TS9/10a,h-j**, which approaches through the *mismatched* transition state **TS9/11a,h-j** for the hindered side which leads to products **11a,h-j** which are enantiomers of **10a,h-j**. Experimentally, the enantioselectivity also varies for different solvents. As rather small differences in activation energies are sufficient to yield significant selectivities, we therefore also modeled solvent effects the conductor-like screening model (COSMO) approach. Then we compare the results for the two small amino acids L-alanine dimethylamide and L-valine dimethylamide with the large amino acids L-*tert.*-leucine dimethylamide and L-neopentylglycine dimethylamide. We conclude that the enantioselectivity increases with the amino acid size. The experiments of Christoffers [87, 108] show that the chiral auxiliaries made of valine, leucine and *tert.*-leucine induce a selectivity up to 78% ee in the metal-free background reaction. In all cases the R configured isomer is the matched product **5**. In the presence of the catalyst $Cu(OAc)_2$ the enantioselectivity increases by 20%. We have expected a high energy difference between the matched and mismatched transition states. We found that the attack of the Michael donor from the side shielded by the amino acid side chain is so much hindered that the attack on the Michael acceptor occurs not from the axis of the square planar geometry and instead from the side of the plane. The plane is defined as the square planar coordination around copper.



Scheme 10: Investigated Michael reactions with different auxiliaries used for the computed enantioselectivities.

4.2.1 L-Alanine (Ala) and L-valine (Val)

This calculations started using the smallest chiral amino acid L-alanine. The difference of the reaction barriers ΔE_A between the matched **TS9a/10a** and mismatched product **TS9a/11a** of 2.7 kJ/mol using the DFT functional B3LYP and TZVP basis set which corresponds to an ee value of 49%. In the case of valine a theoretical prediction is complicated, because of several possible conformations of the amino acid side chain and this brings a high entropic effect for example if the number of accessible conformations is different in both transition states. To calculate this effect it would be necessary to optimise all transition states for each conformation. In the case of an *iso*-propyl group in the amino acid side chain three conformers exist in the matched transition state generated by rotations around the $C_\alpha - C_{iPr}$ bond. The population of these conformers should be all the same because of the

large distance between Michael acceptor and amino acid side chain and small steric effect. This is not the case in the mismatched transition state. The steric effect of the *iso*-propyl group has a high influence on the population of the conformers. The lowest steric effect has the conformer with the high distance of Michel acceptor and donor. The entropic effect in the free energy term of the matched reaction barrier is concluded about $\ln 3 \cdot RT = 2.72$ kJ/mol compared to the mismatched reaction barrier. Comparing the activation energy difference in both stereoisomers with 2.7 kJ/mol (49% ee) of alanine gives valine 1.6 kJ/mol (30% ee) and this is a not expected low results. The steric effect should be larger in case of valine than to alanine, also concluded from the stronger distorted geometry of the mismatched transition states. The optimisation of the mismatched transition state using valine has been repeated in the following way. Starting from **TS9h/10h** the amino acid has been substituted with alanine. The resulting optimised transition state is similar to the previous structure **TS9a/10a**. The result of a higher enantioselectivity with alanine than with valine disagree with the chemical intuition but we have hereupon again checked the calculations and didn't find any errors. The matched and mismatched transition states **TS9a/10a**, **TS9a/11a** and **TS9h/10h** with **TS9h/11h** are shown in Fig. 18.

4.2.2 L-*tert*-Leucine (Tle) and L-neopentylglycine (Npg)

Now we consider the amino acid L-*tert*-leucine as the chiral auxiliary. For this nearly spherical group, entropic effects as considered in the preceding section need not be taken into account. The enantioselectivity calculated by using L-*tert*-leucine should bring a huge difference between the matched and mismatched transition state. The matched and mismatched transition states **TS9i/10i** and **TS9i/11i** are shown in Fig. 19. Using the B3LYP

functional and TZVP basis set gives a value for ΔE_A of 3.8 kJ/mol which leads to an ee of 65% ee. We have observed here a different reaction pathway for the mismatched product. The geometry of the transition state shows that the coordinated aza-enolate on copper is not attacking the Michael acceptor from the axis of the square planar geometry. Instead the Michael acceptor attacks from the side and is coordinated in the square planar geometry pushing out the diketone. The geometry will more precisely be discussed additionally the next section. New experimental data of J. Christoffers show a high chiral induction using L-neopentylglycine (Ngp). The results in case of L-neopentylglycine using B3LYP and full TZVP basis set gives 2.1 kJ/mol difference of the reaction barriers which corresponds to an ee value of 39%. Here an entropic effect similar to valine is expected due to large number of conformers. A lower enantioselectivity than in the *tert*-butyl group was calculated as expected, because the amino side chain is free to move, not interfering with the Michael acceptor. The steric effect of the Michael acceptor and the L-neopentylglycine gets lower than in the case of the *L-tert*-leucine. Therefore the transition state for the disfavoured product shows that L-neopentylglycine side chain is moving away from the Michael acceptor. This is in agreement with the experimental data showing a lower enantioselectivity than in the case of *tert*-leucine. The optimised transition states **TS9j/10j** and **TS9j/11j** for the matched and mismatched product are shown in Fig. 19. Table 3 presents the calculated ΔE_A and resulting enantioselectivities for different amino acids using DFT (B3LYP functional). Table 4 shows the absolute energy results for the reaction barriers for the R matched product and the S mismatched product with the electronic energy, in kJ/mol. The results show that the enantioselectivity compared to the experimental date is underestimate in gas phase calculations. The influence of the chiral auxiliary

is well described qualitatively and the amino acid side chain has a strong influence on the enantioselectivity. Surprisingly is the effect of the ZPVE on the enantioselectivity. The ZPVE decreases the enantioselectivity and in the case of valine is actually an inversion observed (Table 4). The calculations has been checked but we didn't find any error. We think the reason is indicated in the error limit of DFT.

4.2.3 Comparison of the matched and mismatched transition state

Our first suggestion was that the coordination sphere around copper is so rigid that the attack on the Michael acceptor from the side chain hindered by the amino acid is blocked. This was expected as the chiral induction. However we were successful in calculating this transition states for the disfavoured product which proof the exist of this pathway. Now equals have been calculated for different sizes of the amino acids (Fig. 16). We observe that the amino acid side chain bends away from the square planar geometry which gets distorted. The ligands are square planar coordinated in the reactive species (Michael donor **9**). The aza-enolate and the water ligand coordinated to Cu(II) are defined as the square planar coordination sphere. In the matched transition state are the same ligands square planar coordinated around copper(II). The nucleophilic attack from the sterically hindered side of the Michael donor on the Michael acceptor has a large influence on the geometry. We are observing that the Michael acceptor is pushing the second carbonyl group out of the plane and now the Michael acceptor is in the square planar coordination sphere around copper. We compare in this section the out of plane angles in the mismatched transition states with the *original* ligands: aza-enolate and a water molecule as the co-ligand in the plane and in the second case the Michael acceptor. The results are presented

in table 6. For the calculation of the out of plane angle the plane was defined by the nitrogen and oxygen of the six membered ring and copper. Our results show that with increasing size of the amino acid side chain the distortion of the geometry in the mismatched transition state is deepened. The out of plane angle with the Michael acceptor on the other side is decreasing with the size of the amino acid. In case of L-neopentylglycine is the out of plane angle (Michael acceptor in the plane) larger than for *tert.*-leucine despite of the huger size of the amino acid. The reason is that the neopentyl group has the ability to move away from the attacked Michael acceptor. The bond length of the performed C-C bond formation differs considerably in the matched and mismatched transition state (Table 5). The value of this length is smaller in the preferred transition state than in the disfavoured transition state by 0.2 Angstrom. In all cases the bond lengths for the constructing C-C bond in the matched transition states are lower than for the mismatched transition states. We find and a more product like geometry for this case.

The transition states that lead to the two products are different in nature, because an approach of the Michael acceptor from the sterically hindered side requires a reorganisation of the copper coordination sphere. We concluded out of the different geometries of the matched and mismatched transition states that there indeed exist two different reaction channels forming the two different quaternary stereo centers. The question arises now whether there exist additionally a energetically deeper transition state for the matched product with the reorganised coordination sphere around the copper center. Now we want to describe the approach of this investigation. We distinguished in the previous section between the configuration of the two diastereomer transition state: Matched transition state: (*S*)/(*R*), Mis-

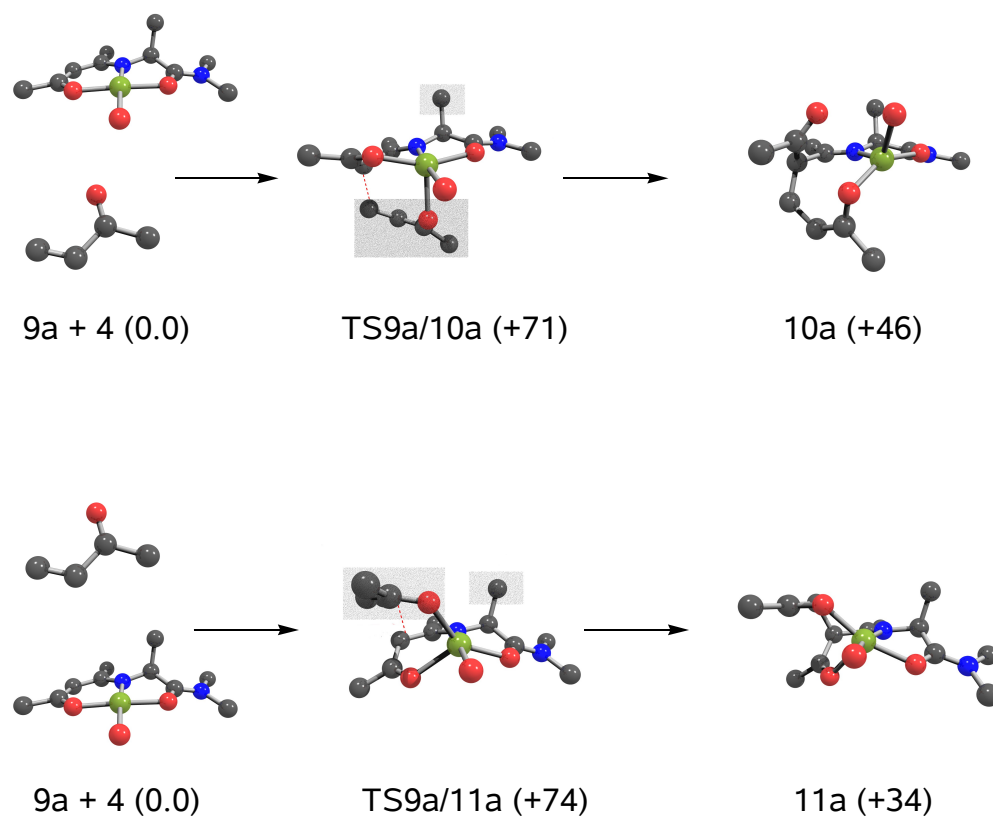


Figure 16: Investigated reaction pathway of C-C bond formation. The preferred and the disfavoured attack of the coordinated aza-enolate on the Michael acceptor has been investigated.

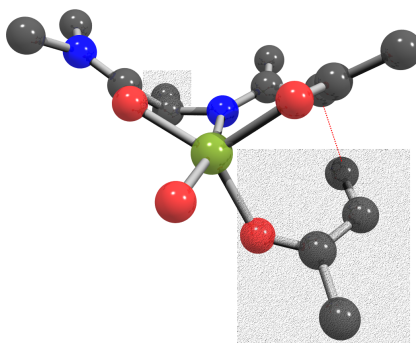


Figure 17: Alternative transition state for the matched transition state **TS9a/10a** with a larger barrier than for the primer showed transition state for the favoured product.

matched transition state: $(S)/(S)$. The first letter signify the configuration of the amino acid and the second letter the configuration of the formed quaternary stereo center. To investigate the possibility of a different reaction channel for the matched product we apply the following procedure. Starting point for this calculation has been the mismatched transition state **9a/11a**. The the configuration at the amino acid has been chained and the transition state remain optimised. This molecule exhibit the following configuration: $(R)/(S)$. Due to the similar energy of two enantiomers, we assume that the energy of the located transition state should be equal to one with the configuration: $(S)/(R)$ which is the similar to **9a/10a**. Indeed we successfully located such a transition state presented in Fig. 17. Surprisingly is this stationary point 71 kJ/mol higher in energy then the previous described transition state **TS9a/10a** due to the arisen sterical interaction. The lower distance between two methyl group: amino acid side chain and the methyl group of the 1,3-diketone, increase the sterical interaction and the energy

of the transition state. This transition state is not relevant because of the large reaction barrier. To check this results the transition state optimisation has been repeated, replacing the amino acid with glycine. In the same way was the mismatched transition state been reoptimised with glycine instead of alanine. The resulting geometries are both without any energy difference. Already the start geometry of both optimisations differs with 45.23 kJ/mol. We conclude the additional sterical interaction of two methyl groups as the reason for the huge reaction barrier.

4.3 Solvation effects on the enantioselectivity

All previous calculations were performed in the gas phase. The experiments of Christoffers show the best results for the enantioselectivity in solvent (acetone, dielectric constant=20.7) are up to 99% ee. Solvents with smaller polarity like dichlormethane and toluol produce lower enantioselectivity of this reaction in the experiments. All optimisations of minima and transition states in this section are performed using the continuum model COSMO [109–118] implemented in Gaussian03. The optimised geometries of minima and transition states for all molecules in the gas phase were taken as the start geometry for the COSMO optimisation. To check this data single point calculations have been made with all structures using the TURBOMOLE implemented COSMO model. The calculated solvation energies are presented in table 7. The observed deviation in the solvation energies of the COSMO model is up to 3 kJ/mol and in some cases up to 10 kJ/mol. TURBOMOLE and Gaussian have slightly different implementations of the COSMO model. This is a reason for the different solvent energies calculated with both program packages. Table 8 gives the results for the reaction barrier differences ΔE_A and the resulting enantioselectivities in gas phase and COSMO imple-

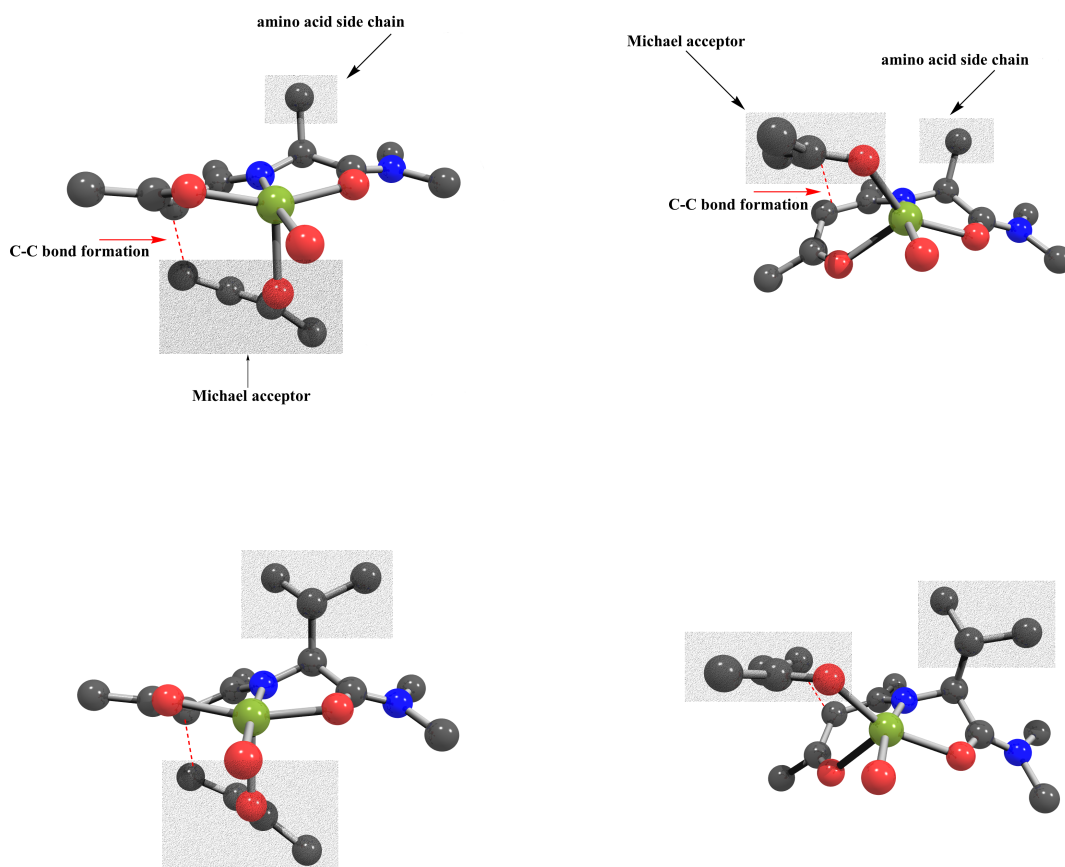


Figure 18: This figure presents the optimised transition states. On the left side are the transition states for the matched and on the right side for the mismatched products. Left side: **TS9a/10a**, **TS9h/10h**. Right side: **TS9a/11a** **TS9h/11h**.

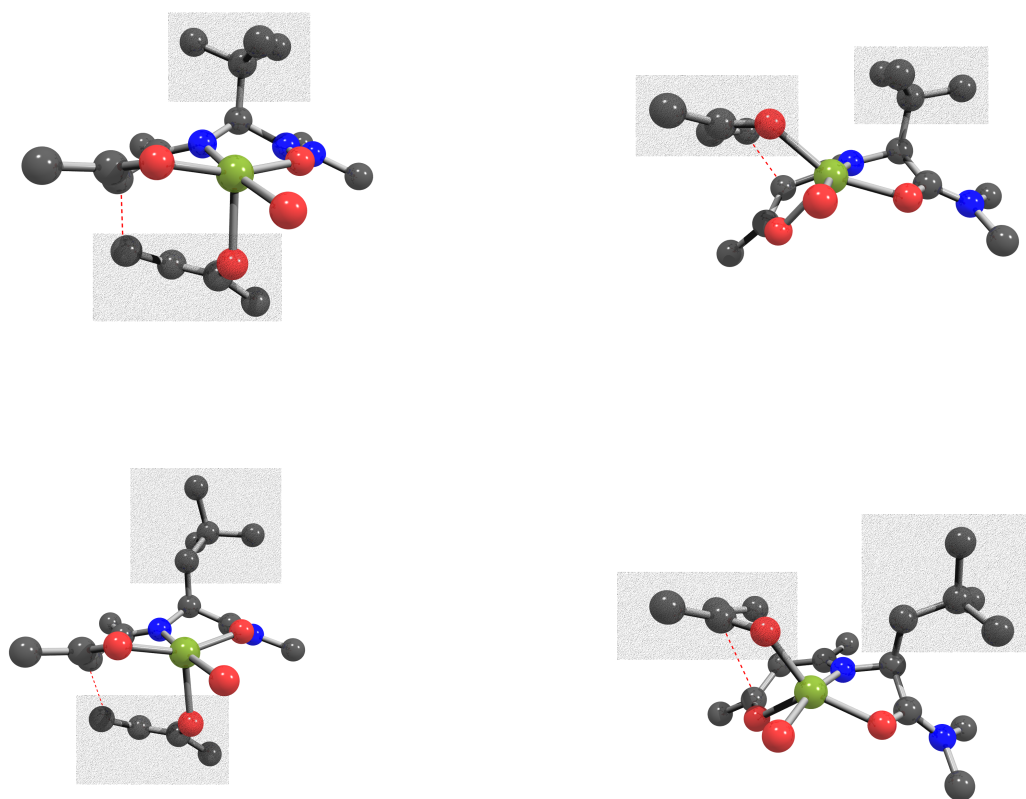


Figure 19: This figure presents the optimised transition states. On the left side are the transition states for the matched and on the right side for the mismatched products. Left side: **TS9i/10i**, **TS9j/10j**. Right side: **TS9i/11i**, **TS9j/11j**.

mented in Gaussian. The absolute barriers are shown in table 9. The results for the enantioselectivity with different sizes of amino acids in the gas phase in the previous section described show an underestimate enantiomeric excess compared to the experiments. Introducing solvent effects in the calculation of enantioselectivity gives results approximately to the experiment. But the accuracy of the COSMO model is insufficient to be used for the exact calculation of solvent effects on the enantioselectivity. The following presented results are calculated with COSMO implemented in Gaussian. The value ΔE_A in case of alanine increase from 3 kJ/mol in the gas phase to 8 kJ/mol in solvent which leads to an ee of 49% in gas phase and 92% ee in solvent. In case of valine the account of ΔE_A in gas phase of 2 kJ/mol (30% ee) increases to 11 kJ/mol (98% ee). The largest effect feature the *tert.*-leucine used pathway with 4 kJ/mol (65% ee) in gas phase and 14 kJ/mol (99% ee) in acetone. The solvation energy of the matched and mismatched transition state show differences of 6-11 kJ/mol.

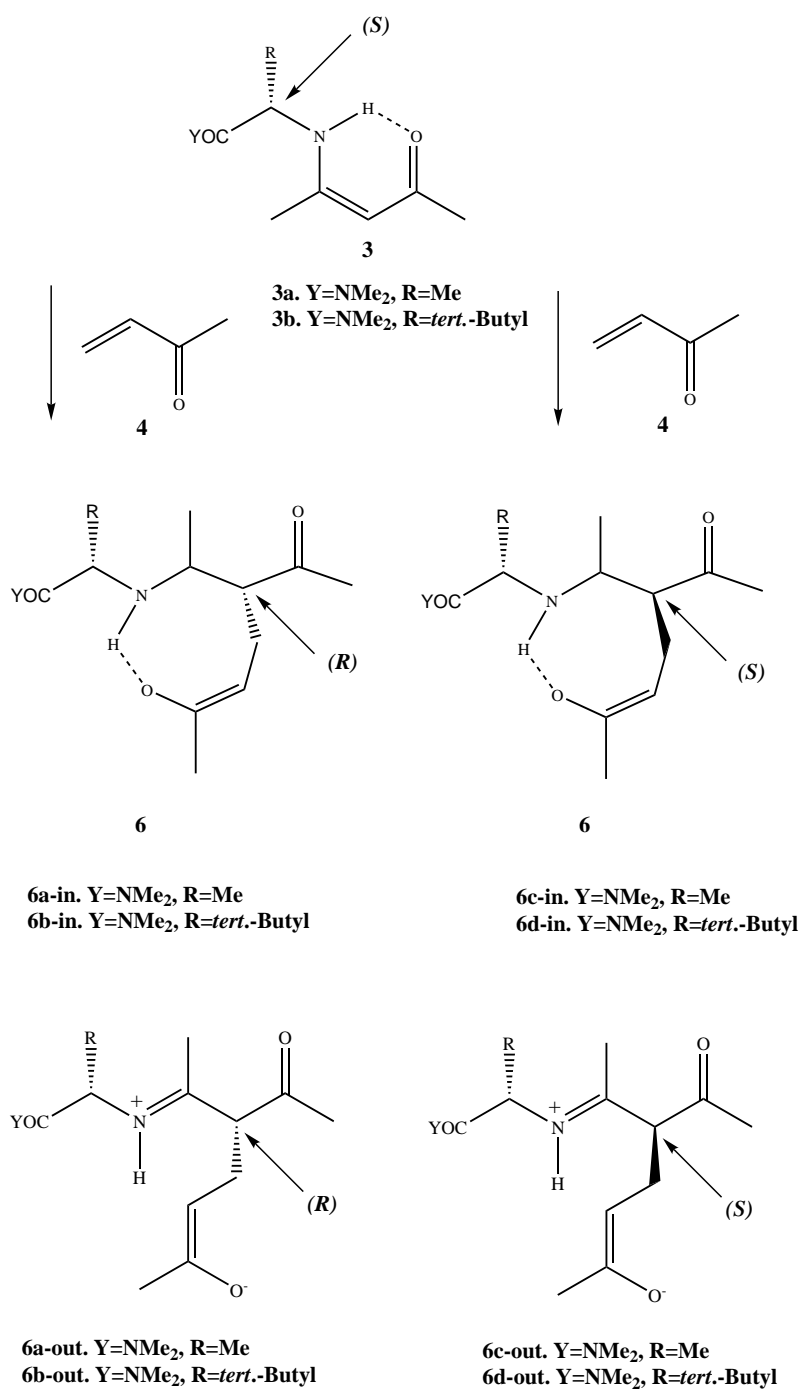
To investigate possible reasons we have been looked at the electrostatic potential map of both transition states. The electrostatic potential and the surface area differs not much between both product isomers transition state. This is not surprising because of the similar charge and surface area of both structures. We still have no decisive explanation why polar solvents increase enantioselectivity. But already small differences in the reaction barriers have a huge effect on the enantioselectivity. Also the exact absolute energy barriers of both reaction pathways increases in solvent. The solvation energy in case of the pathway using alanine is in the sum of Michael donor **9a** (188 kJ/mol) and Michael acceptor **4** (25 kJ/mol) with 212 kJ/mol larger than for the transition state **TS9a/10a** (185 kJ/mol) and **TS9a/11a** (180 kJ/mol). This increasing absolute reaction barriers in gas phase and solvent

has been also observed in the pathways using other amino acids. We can conclude that the COSMO accuracy is not precise enough to calculate absolute enantioselectivity with solvent effects. A higher exactness of about 0.1 kJ/mol is necessary for the precise calculation of solvent effects on the enantioselectivity. The additional difficulty of the convergence in COSMO optimisations due to the roughness of the energy potential surface increases the error of these results up to 2 kJ/mol. We can conclude that the introduction of solvent effects in the calculations successfully describes the experimental enantioselectivities.

4.4 Metal-free background reaction

In the previous section 3.2 has been the preferred folded transition state in the metal free background reaction described which owns an important intramolecular hydrogen bond. The existence of such a transition state has been proved by experiments (section 3.3). Now we focus on the enantioselectivity of this metal-free background reaction in gas phase. The calculations have been performed similar to the previous section. We have been locating the folded transition states for the matched and mismatched product using the amino acids alanine and *tert.*-leucine as chiral auxiliaries (**3a** and **3b**) (Scheme 11). In gas phase is just this transition state locatable. A higher chiral induction in case of the *tert.*-leucine is expected than with alanine and has been also calculated but unfortunately for the opposite (*S*) enantiomer than in experiments. The difference in the activation energies is in the case of alanine computed to 0.9 kJ/mol and for the *tert.*-leucine to 2.4 kJ/mol. We have been computing indeed a higher chiral induction increasing with the size of the amino acid (Table 10). But the favoured configured enantiomer is not similar with the experiment. We have to mention here that the accuracy

of the calculations is especially in case of a low enantiomeric excess not high enough to give precisely results. We located one the zwitterionic transition state including solvent effects. Indeed the reaction barrier crossing the folded transition state **TS3a/6a-in** increases in solvent. The activation energy of 92.3 kJ/mol increases to 117.4 kJ/mol. Transition state **TS-3a/6a-out** is not possible to be located in gas phase due to the zwitterionic structure. An optimisation in solvent (acetone) using COSMO gives a located transition state with a barrier of 91.4 kJ/mol which is in magnitude to the previous folded transition state (Table 11). Due to this result we can conclude that the folded transition state is preferred in gas phase but in solvent the zwitterionic structure is also feasible. Like mentioned before the experiment of section 3.2 exclude the zwitterionic transition state. In any case is the copper catalyzed reaction the preferred pathway in contrast to all other presented paths. The folded transition states which has been located for alanine and *tert.*-leucine are presented in Fig. 20. The only zwitterionic transition state which has been successful located in solvent is **TS3a/6a-out** (Scheme 11).



Scheme 11: Investigated metal-free background reaction.

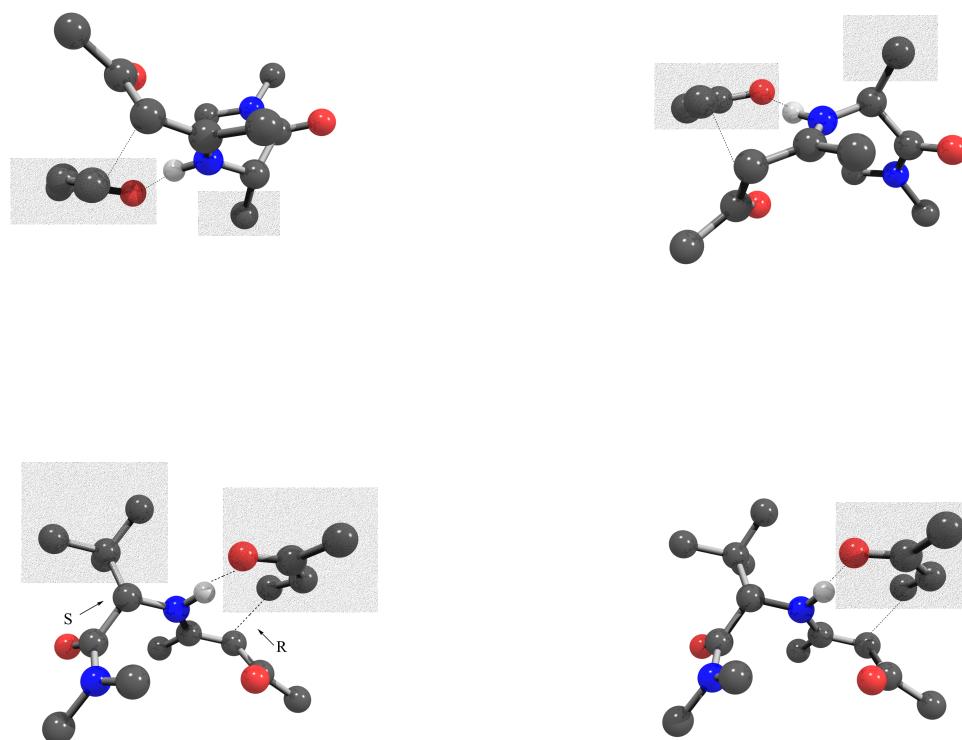


Figure 20: Optimised transition states of both product isomers using alanine and *tert.*-leucine as the chiral auxiliary. The favoured isomer both case is here the R isomer in contrast to the experimental data.

5 Computational details

Total energies were obtained by density functional calculations performed with the Gaussian03 [91] and TURBOMOLE [92, 93] quantum chemical program packages. TZVP basis sets [94] have been used throughout. In all cases the B3LYP exchange correlation functional [55–60] has been used. For the reaction profiles, the minima and transition states were characterised by a harmonic vibrational analysis. We have used the B3LYP-VWN5 functional [119] in which the VWN5 (developed by Vosko, Wilk, and Nusair) functional is used as the local correlation part. In contrast to TURBOMOLE B3LYP implemented in Gaussian03 uses the VWN functional. In this case a modification of the source code of Gaussian03 is necessary to get the B3LYP-VWN5 functional. The computational methods for the calculation of enantioselectivity and solvent effects has been already described in section 4.2.

We performed test calculation to study the influence of relativistic effects on the main reaction barrier of C-C bond formation. These calculations have been performed scalar relativistically (per direct perturbation theory) [120, 121] using the TURBOMOLE package [92, 93]. The investigated pathway is the nucleophilic attack of the coordinated aza-enolate on copper (**9b**) on Michael acceptor **4**. The reaction barrier has been computed without relativistic effects to 64.92 kJ/mol and including relativistic effects to 67.17 kJ/mol. The relativistic effect on the barrier has a value of 2.25 kJ/mol. This effect is small and due to this results relativistic effects has not been taken into account in all further optimisations.

We have used a full DFT (B3LYP) calculation to optimise all minima and transition states. The zero point vibrational energy has been added to the electronic energy to obtain reaction and activation enthalpies. If this has not been done it is described in the correspondence sections. The transition

states have been in the following way preoptimised. The RI-option (*resolution of identity*) of the TURBOMOLE V5-7 package has been used in a scan calculation along the reaction coordinate forming the C-C bond. For this case several geometry optimisations has been made with RI-BP86. Using the highest energy geometry a full optimisation has been performed with Gaussian03 with the B3LYP TURBOMOLE functional. The optimisation of transition states of open shell systems is not yet possible with TURBOMOLE. It was not possible to preoptimise the transition states using the QST2/QST3 implementation in Gaussian.

We performed test calculations using a small basis set to reduce computational effort and study the influence of this different basis set on a reaction barrier. The model system is the reaction pathway of C-C bond formation between a coordinated enamine and methylvinylketone (**7a** + **4** → **TS7a/8a** → **8a**). First we used TZVP basis set for all atoms and second a mixed small basis set (TZVP for all atoms in the reactive part excluding the amino acid side chain, SVP for the carbon atoms and SV basis set for the hydrogen atoms in the amino acid side chain). The reaction barrier calculated with TZVP basis set was computed to 98.99 kJ/mol and with the small basis set to 98.95 kJ/mol (electronic energy without ZPVE). The resulting difference of the reaction barrier calculated with the large and small basis set is 0.05 kJ/mol. We conclude that it is useful to take this small basis set for the preoptimisations of large molecules due to the small difference compared with the full TZVP basis set. Similar test calculation have been performed for the reaction pathway of C-C bond formation using *tert.*-leucine as the amino acid. The transition states for the matched **TS9i/10i** and mismatched product **TS9i/11i** were optimised using first full TZVP basis set and secondly

Computational details

a small basis set described previously. The difference of the reaction barriers for both stereoisomers calculated with TZVP basis set for all atoms was computed to 3.81 kJ/mol and using the small basis set to 4.03 kJ/mol. The resulting displacement of the calculation with a small basis set has been computed to 0.22 kJ/mol.

6 Summary

This PhD thesis investigates quantum chemical (DFT) studies on the copper(II) catalyzed Michael reaction. The reaction mechanism and the molecular process leading to the high enantioselectivity has before not been clarified by either experiment or theory at the onset of our work. We have investigated feasible reaction pathways and intermediates to elucidate the mechanism. Methylvinylketone, acting as the Michael acceptor reacts with an enamine (Michael donor), synthesized from a 1,3-diketone and an amino acid. Experimentally, copper(II)diacetate and a chiral auxiliary (amino acid) must be introduced to achieve high enantioselectivity. We have investigated the role of the amino acid in the molecular process of the chemoselectivity. We have calculated reaction barriers for three different pathways: (1) metal-free background reaction, (2) C-C bond formation of a coordinated enamine on copper and (3) C-C bond formation of a coordinated aza-enolate to copper. Experiments show that also a metal-free reaction exists, yielding a small but reasonable enantioselectivity. Therefore, we have to expect the existence of a metal-free background reaction despite the use of the catalyst. Our calculations show that an intramolecular proton shift exists in the transition state. This path, with a computed barrier of 97 kJ/mol (**TS3a/6**), would be favoured over a zwitterionic transition state, which can be not located in gas phase. Calculations on the enantiomeric excess (ee) with the chiral auxiliaries alanine and *tert.*-leucine were performed. Theoretical calculations together with experiments showed that our proposed transition state is plausible.

We propose that the refined enamine first coordinates to the copper-center. Then, two possible pathways for the further reaction exist (2) and (3): The computed barrier of path (2) (94 kJ/mol (**TS7a/8a**)) has the same mag-

nitude as the metal-free variant of the reaction. We found that the lowest barrier for this reaction is given by reaction path (3), which is the nucleophilic attack of an aza-enolate coordinated on three ligand sites on the copper(II) **9a**. The fourth coordination site is filled with the acetic acid, giving the lowest computed reaction barrier (**TS9a/10a**) of 71 kJ/mol. The enamine is coordinating on copper with an acetate molecule as the co-ligand. The intramolecular proton shift from the enamine nitrogen to the acetate oxygen ($7c \rightarrow 9a$) is exothermic with 58 kJ/mol leading to the square planar coordinated reactive species (**9a**) which is most reactive. We investigated other co-ligands in species **9** (ammonia, ethanol, methanol, acetone, and water) and acetic acid causes the lowest barrier of this main reaction path. Additionally, we investigated an *outside attack* of the Michael donor meanwhile the Michael acceptor is not coordinated on copper. But this highly polar transition state is not preferred, neither in gas phase nor including solvent effects by using COSMO. The resulting catalytic cycle for the computed mechanism is shown in scheme **9**.

In all cases, the N-H bond is broken either before or during C-C bond formation, and no imminium ion intermediates are performed. These pathways are not possible for secondary enamines which are formed if one starts e.g. from a N-methylated amino acid. Indeed, in an experiment we suggested by the present work, no reactivity has been observed in such a case, either for the metal-free background reaction or in the presence of $\text{Cu}(\text{OAc})_2$ [86].

Our predictions were confirmed by experiments, where ESI-Mass spectroscopy indicate the existence of a coordinated aza-enolate on copper(II).

The main feature of this reaction is the high enantioselectivity due to the use of chiral amino acids as auxiliaries for the reaction. We proposed the following mechanism for the chiral induction: The amino acid side chain is oriented

axial out of the square planar coordination sphere around copper. The nucleophilic attack from the Michael donor on the Michael acceptor occurs from the opposite side of the plane, sterically not hindered by the amino acid side chain. We calculated the enantioselectivity with amino acids with different sizes of the side chains. We located transition states which are eventually leading to both enantiomers (Scheme **10**) and used the corresponding energy difference for the calculation of the enantiomeric excess (ee). Alanine, valine *tert.*-leucine and neo-pentylglycine were used as the chiral auxiliary (Table 3). In our calculations, we observed the highest chiral induction using *tert.*-leucine as the chiral auxiliary with an energy difference between both possible transition states of 3.8 kJ/mol (65 % ee). This tendency of increasing enantiomeric excess with the amino acid size is shown in the calculations, but all of these enantioselectivities are underestimated compared to the experimental data. We found out that the geometry of the enantiomer transition states are quite different in nature showing a strong distortion from the square planar coordination in case of the disfavoured product. We have to mention that all of the calculations were performed in gas phase while experiment show the best results in acetone as a solvent. Therefore, we introduced solvation effects simulated with the continuum model COSMO. All transition states were optimised including solvent effects. The results for the calculated enantioselectivities in the gas phase compared to the solvent acetone and experimental data is shown in Table 8. The energy difference increases between the reaction barriers of both transition states for example in case of *tert.*-leucine from 3.8 kJ/mol (65% ee) in gas phase to 14 kJ/mol (99% ee) in solvent.

The solvent decreases the reactivity (because the compact transition states have a lower solvation energy than the starting material) but increase the

Summary

enantioselectivity. Despite the insufficient accuracy of optimisations performed using the continuum model and DFT, we can show with these calculations, that the proposed mechanism, supported by theoretical calculations, can account for the experimental effective high enantioselectivity of this reaction.

This work has contributed to an understanding of the reaction mechanism and how chiral information is transferred from the auxiliary to the new asymmetric carbon center.

7 Tables

Ligand L	ΔE in kJ/mol
7a \rightarrow 8a	94
7b + 4 \rightarrow 7b₄	-133
7b₄ \rightarrow 8b	103
7c \rightarrow 8c	(50)
7d + 4 \rightarrow 7d₄	-106
7d₄ \rightarrow 8d	110
9a \rightarrow 10a	70.9
9b \rightarrow 10b	64.9
9c \rightarrow 10c	68.8
9d \rightarrow 10d	71.8
9e \rightarrow 10e	72.7
9f \rightarrow 10f	75.1

Table 1: Reaction barriers of C-C bond formation (without zero-point vibrational energy (ZPVE)) of all investigated pathways of a coordinated aza-enolate on copper(II).

structure	$E^{[a]}$	$E^{[b]}$	$E^{[c]}$	$E^{[d]}$	$E^{[e]}$
9a + 4	209.1	211.9			
TS-outside	207.8	205.3	118.6	123.7	125.1
TS-inside (TS7a/9a)	179.8	185.3	70.9	100.5	97.4

Table 2: The first two columns contain solvation energies and the following three columns contain activation energies ($E(\text{TS}) - E(9\text{a}+4)$): [a], [b]: solvation energies calculated with the PCM and COSMO model, [c]: activation energies in gasphase, [d], [e]: activation energies calculated with the PCM and COSMO model

amino acid ^[a]	ΔE_A	ee
Ala	2.7	49%
Val	1.6	30%
Tle	3.8	65%
Npg	2.1	39%

Table 3: Reaction barriers differences ΔE_A (electronic energy without zero-point vibrational energy) (in kJ/mol) and derived enantioselectivity of several pathways using [a] different amino acids for the chiral auxiliaries using the B3LYP functional and TZVP basis set.

amino acid ^[a]	TS	E_A	$E_A + \text{ZPVE}$
Ala	9a/10a	70.9	77.7
Ala	9a/11a	73.6	78.0
Tle	9i/10i	67.7	76.8
Tle	9i/11i	71.5	78.2
Val	9h/10h	69.6	77.4
Val	9h/11h	71.2	75.1

Table 4: Results of the absolute reaction barriers using [a] different amino acids in the chiral auxiliaries in kJ/mol. TS describes the stereoisomer of the constructed product in the transition state.

amino acid ^[a]	C-C bond length	
	in TS9/10	in TS9/11
Ala	1.88	2.05
Val	1.88	2.09
Tle	1.88	2.10
Npg	1.90	2.06

Table 5: C-C bond lengths for the optimised transition states of the matched and mismatched products using [a] different amino acids in the chiral auxiliaries. The results in the third column are without zero point vibrational energy correction (ZPVE) and the fourth column gives the reaction barrier with ZPVE.

out of plane angle		
	original	MA
Ala	40.02°	35.23°
Val	25.11°	11.84°
Tle	21.58°	6.52°
Npg	32.58°	26.11°

Table 6: Results of the out of plane angles of the square planar coordination sphere of copper(II) in the mismatched transition states with different amino acids. **L** means the type of ligands for the square planar coordination. Original means the four ligands are the aza-enolate and the water molecule. MA means that instead of the second ketone of the aza-enolate is the Michael acceptor **4** used as the ligand.

molecule	$E_{solvent}^{[a]}$
4+9b	213
TS9a/10a	185
TS9a/11a	180
10a	176
11a	176
4+9h	208
TS9h/10h	180
TS9h/11h	171
10h	170
11h	174
4+9i	206
TS9i/10i	177
TS9i/11i	166
10i	190
11i	190

Table 7: Calculated solvation energies (electronic energy without zero-point vibrational energy) [a] in kJ/mol using COSMO implemented in Gaussian out of the difference between a full COSMO optimisation and the gas phase result.

amino acid ^[a]	$\Delta E_A^{[b]}$	$ee^{[b]}$	$\Delta E_A^{[c]}$	$ee^{[c]}$	$\Delta E_A^{[d]}$	$ee^{[d]}$	$ee(Exp.)$
Ala	2.7	49%	8	92%	7.6	91%	-
Val	1.6	30%	11	98%	6.5	86%	99%
Tle	3.8	65%	14	99%	11.5	98%	99%

Table 8: Reaction barriers (electronic energy without zero-point vibrational energy) differences of both stereo isomers ΔE_A and the resulting enantioselectivity using [a] different amino acids in the chiral auxiliaries, [b] in gas phase, [c] COSMO implemented in Gaussian [d] COSMO implemented in TURBOMOLE using single point calculations compared to the experimental enantioselectivities.

amino acid ^[a]	pathway	$E^{[b]}$	$E^{[c]}$
Ala	9a + 4 → 10b	70.9	97.5
Ala	9a + 4 → 11b	73.6	105.6
Val	9h + 4 → 10h	69.6	97.9
Val	9h + 4 → 11h	71.2	108.0
Tle	9i + 4 → 10i	67.7	96.1
Tle	9i + 4 → 11i	71.5	109.8

Table 9: Absolute reaction barriers (electronic energy without zero-point vibrational energy) for the pathways of both stereo isomers using [a] different amino acids in the chiral auxiliaries, in [b] gas phase and [c] COSMO using Gaussian03.

amino acid	$\Delta E_{TS}(kJ/mol)$	EE (%)
Ala	0.93	18.55
Tle	2.41	45.13

Table 10: Results for the enantioselectivity of the C-C bond formation in the metal-free background reaction with different chiral auxiliaries

structure	$E_{ac}^{[a]}$	$E_{ac}^{[b]}$
TS3a/6a-in	92.3	117.4
TS3a/6c-in	91.3	-
TS3a/6a-out	-	91.4

Table 11: Results of the absolute barriers [a]: gas phase and [b] using COSMO.

8 References

References

- [1] B. E. Rossiter, N. M. Swingle, *Chem. Rev.* 92 (1992) 771.
- [2] J. Leonard, E. Diez-Barra, S. Merino, *Eur. J. Org. Chem.* (1998) 2051.
- [3] M. P. Sibi, S. Manyem, *Tetrahedron* 56 (2000) 8033.
- [4] N. Krause, A. Hoffmann-Röder, *Synthesis* 2 (2001) 171.
- [5] S. C. Jha, N. N. Joshi, *Arkivoc* VII (2002) 167.
- [6] Article *Michael Addition*, in: *Encyclopedia of Catalysis*, I. T. Horvath, Wiley-VCH, Weinheim (2003).
- [7] *Modern Aldol Reactions*, R. Mahrwald, Wiley-VCH, Weinheim (2004).
- [8] K. C. Nicolaou, G. Vassilikogiannakis, W. Mägerlein, R. Kranich, *Angew. Chem. Int. Ed.* 40 (2001) 2482.
- [9] R. B. Woodward, F. Sondheimer, D. Taub, K. Heusler, W. M. McLamore, *J. Am. Chem. Soc.* 74 (1952) 4223.
- [10] T. Mizoroki, K. Mori, A. Ozaki, *Bull. Chem. Soc. Jpn.* 44 (1971) 581.
- [11] R. F. Heck, J. J. P. Nolley, *J. Org. Chem.* 37 (1972) 2320.
- [12] A. de Meijere, F. E. Meyer, *Angew. Chem. Int. Ed. Engl.* 33 (1994) 2379.
- [13] *Metal-Catalyzed Cross-Coupling Reactions*, A. de Meijere, F. Diederich, Wiley-VCH, Weinheim (2004).

- [14] E. D. Bergmann, D. Ginsburg, R. Pappo, *Org. React.* 10 (1959) 179.
- [15] *Topics in Stereochemistry: 19*, S. H. Wilen, Wiley-VCH, Weinheim (1989).
- [16] R. D. Little, M. R. Masjedizadeh, O. Wallquist, J. I. McLoughlin, *Org. React.* 47 (1995) 315.
- [17] R. Pearson, *Acc. Chem. Res.* 26 (1993) 250.
- [18] *Modern Organocopper Chemistry*, N. Krause, Wiley-VCH, Weinheim (2002).
- [19] A. Alexakis, C. Benhaim, S. Rosset, M. Humam, *J. Am. Chem. Soc.* 124 (2002) 5262.
- [20] M. T. Reetz, A. Gosberg, D. Moulin, *Tetrahedron Letters* 43 (2002) 1189.
- [21] T. Kommenos, *Liebigs Ann. Chem.* 218 (1883) 145.
- [22] L. Claisen, *J. Prakt. Chem.* 35 (1887) 413.
- [23] A. Michael, *J. Prakt. Chem.* 35 (1887) 349.
- [24] A. Michael, *J. Prakt. Chem.* 36 (1887) 113.
- [25] A. Michael, O. Schulthess, *J. Prakt. Chem.* 45 (1891) 55.
- [26] A. Michael, *Chem. Ber.* 27 (1894) 2126.
- [27] A. Michael, *Chem. Ber.* 33 (1900) 3731.
- [28] I. Denissova, L. Barriault, *Tetrahedron* 59 (2003) 10105.

- [29] C. J. Douglas, L. E. Overman, Proc. Natl. Acad. Sciences U.S.A. 101 (2004) 5363.
- [30] J. Christoffers, A. Baro, Angew. Chem. Int. Ed. 42 (2003) 1688.
- [31] *Quarternary Stereocenters*, J. Christoffers and A. Baro, Wiley-VCH, Weinheim (2005).
- [32] J. Christoffers, A. Mann, Angew. Chem. 112 (2000) 2871.
- [33] J. Christoffers, H. Scharl, Eur. J. Org. Chem. (2002) 1505.
- [34] J. Christoffers, H. Scharl, W. Frey, A. Baro, Org. Lett. 6 (2004) 1171.
- [35] Y. Hamashima, D. Hotta, M. Sodeoka, J. Am. Chem. Soc. 124 (2002) 11240.
- [36] J. Christoffers, Eur. J. Org. Chem. 1998 (1998) 1259.
- [37] J. Christoffers, J. Chem. Soc., Perkin Trans. 1 (1997) 3141.
- [38] J. Christoffers, Chem. Eur. J. 9 (2003) 4862.
- [39] J. Christoffers, A. Mann, Angew. Chem. Int. Ed. 39 (2000) 2752.
- [40] S. Pelzer, T. Kauf, C. van Wüllen, J. Christoffers, J. Organomet. Chem. 684 (2003) 308.
- [41] J. Christoffers, Chem. Commun. (1997) 943.
- [42] J. Christoffers, Synlett 6 (2001) 723.
- [43] J. Christoffers, A. Mann, Angew. Chem. Int. Ed. 40 (2001) 4591.
- [44] J. Christoffers, H. Scharl, W. Frey, A. Baro, Eur. J. Org. Chem. (2004) 2701.

- [45] J. Christoffers, A. Mann, Chem. Eur. J. 7 (2001) 1014.
- [46] J. Christoffers, T. Werner, S. Unger, W. Frey, Eur. J. Org. Chem. (2003) 425.
- [47] J. Christoffers, B. Kreidler, H. Oertling, S. Unger, W. Frey, Synlett 4 (2003) 493.
- [48] J. Christoffers, B. Kreidler, S. Unger, W. Frey, Eur. J. Org. Chem. (2003) 2845.
- [49] J. Comelles, M. Moreno-Manas, E. Perez, A. Roglans, R. M. Sebastian, A. Vallibera, J. Org. Chem. 69 (2004) 6834.
- [50] A. Alexakis, Pure Appl. Chem. 74 (2002) 37.
- [51] *A Chemist's Guide to Density Functional Theory*, W. Koch and M. C. Holthausen, Wiley-VCH, Weinheim (2001).
- [52] P. Hohenberg, W. Kohn, Phys. Rev. B 136 (1964) 864.
- [53] W. Kohn, L. J. Sham, Phys. Rev. A 140 (1965) 1133.
- [54] D. M. Ceperly, B. J. Adler, Phys. Rev. Lett. 45 (1980) 566.
- [55] A. D. Becke, J. Chem. Phys. 98 (1993) 5648.
- [56] A. D. Becke, J. Chem. Phys. 107 (1997) 8554.
- [57] J. P. Perdew, Phys. Rev. B 33 (1986) 7406.
- [58] C. Lee, W. Yang, R. G. Parr, Phys. Rev. B 37 (1988) 785.
- [59] P. J. Stephens, F. J. Devlin, C. F. Chabalowski, M. J. Frisch, J. Phys. Chem. 98 (1994) 11623.

- [60] A. D. Becke, *Phys. Rev. A* 38 (1988) 3098.
- [61] M. R. Nyden, G. Petersson, *J. Chem. Phys.* 75 (1981) 1843.
- [62] J. W. Ochterski, G. A. Peterrson, J. Montgomery, *J. Chem. Phys.* 104 (1996) 2598.
- [63] N. Rega, M. Cossi, V. Barone, *J. Am. Chem. Soc.* 119 (1997) 12962.
- [64] C. W. Bauschlicher, H. Partridge, *Chem. Phys. Lett.* 239 (1995) 246.
- [65] R. Ahlrichs, F. Furche, S. Grimme, *Chem. Phys. Lett.* 325 (2000) 317.
- [66] A. J. Cohen, N. C. Handy, *Chem. Phys. Lett.* 316 (2000) 160.
- [67] B. A. Murtagh, R. W. H. Sargent, *Comp. J.* 13 (1970) 185.
- [68] W. C. Davidon, *Comp. J.* 10 (1968) 406.
- [69] D. F. Shanno, *Math. Comp.* 24 (1970) 647.
- [70] H. B. Schlegel, *Theoret. Chim. Acta* 66 (1984) 333.
- [71] H. B. Schlegel, *J. Comput. Chem.* 3 (1982) 214.
- [72] J. Baker, *J. Comput. Chem.* 7 (1986) 385.
- [73] T. A. Halgren, W. N. Lipscomp, *Chem. Phys. Lett.* 49 (1977) 225.
- [74] K. Müller, *Angew. Chem.* 92 (1980) 1.
- [75] S. Bell, J. S. Crighton, *J. Chem. Phys.* 80 (1984) 2464.
- [76] C. Peng, H. B. Schlegel, *Isr. J. Chem.* 33 (1993) 449.
- [77] K. Fukui, *J. Phys. Chem.* 74 (1970) 4161.

- [78] K. Fukui, *Acc. Chem. Res.* 14 (1981) 363.
- [79] C. Gonzalez, H. B. Schlegel, *J. Chem. Phys.* 90 (1989) 2154.
- [80] C. Gonzalez, H. B. Schlegel, *J. Phys. Chem.* 94 (1990) 5523.
- [81] J. Tomasi, M. Persico, *Chem. Rev.* 94 (1994) 2027.
- [82] L. Onsager, *J. Am. Chem. Soc.* 58 (1963) 1486.
- [83] M. Cossi, V. Barone, R. Cammi, J. Tomasi, *Chem. Phys. Lett.* 255 (1996) 327.
- [84] J. Andzelm, C. Kölmel, A. Klamt, *J. Chem. Phys.* 103 (1995) 9312.
- [85] V. Barone, M. Cossi, J. Tomasi, *J. Chem. Phys.* 107 (1997) 3210.
- [86] J. Christoffers, C. L. Diedrich, private communication.
- [87] J. Christoffers, A. Mann, *Angew. Chem. Int. Ed.* 39 (2000) 2752.
- [88] J. Christoffers, F. Fabretti, C. L. Diedrich, private communication.
- [89] J. Christoffers, K. Schuster, *Chirality* 15 (2003) 777.
- [90] J. Borowka, C. van Wüllen, *J. Organomet. Chem.* 691 (2006) 4474.
- [91] M. J. Frisch, G. W. Trucks, H. B. Schlegel, G. E. Scuseria, M. A. Robb, J. R. Cheeseman, J. A. Montgomery, Jr., T. Vreven, K. N. Kudin, J. C. Burant, J. M. Millam, S. S. Iyengar, J. Tomasi, V. Barone, B. Mennucci, M. Cossi, G. Scalmani, N. Rega, G. A. Petersson, H. Nakatsuji, M. Hada, M. Ehara, K. Toyota, R. Fukuda, J. Hasegawa, M. Ishida, T. Nakajima, Y. Honda, O. Kitao, H. Nakai, M. Klene, X. Li, J. E. Knox, H. P. Hratchian, J. B. Cross, V. Bakken, C. Adamo,

- J. Jaramillo, R. Gomperts, R. E. Stratmann, O. Yazyev, A. J. Austin, R. Cammi, C. Pomelli, J. W. Ochterski, P. Y. Ayala, K. Morokuma, G. A. Voth, P. Salvador, J. J. Dannenberg, V. G. Zakrzewski, S. Dapprich, A. D. Daniels, M. C. Strain, O. Farkas, D. K. Malick, A. D. Rabuck, K. Raghavachari, J. B. Foresman, J. V. Ortiz, Q. Cui, A. G. Baboul, S. Clifford, J. Cioslowski, B. B. Stefanov, G. Liu, A. Liashenko, P. Piskorz, I. Komaromi, R. L. Martin, D. J. Fox, T. Keith, M. A. Al-Laham, C. Y. Peng, A. Nanayakkara, M. Challacombe, P. M. W. Gill, B. Johnson, W. Chen, M. W. Wong, C. Gonzalez, J. A. Pople, Gaussian 03, Revision C.02, Gaussian, Inc., Wallingford, CT, 2004.
- [92] TURBOMOLE (version 5.7) is a quantum chemical program package distributed by the university of Karlsruhe. The integration grids used in the density functional calculations are described in [93].
- [93] O. Treutler, R. Ahlrichs, *J. Chem. Phys.* 102 (1995) 346.
- [94] A. Schäfer, C. Huber, R. Ahlrichs, *J. Chem. Phys.* 100 (1994) 5829.
- [95] V. Barone, M. Cossi, *J. Phys. Chem. A* 102 (1998) 1995.
- [96] M. Cossi, N. Rega, G. Scalmani, V. Barone, *J. Comput. Chem.* 24 (2003) 669.
- [97] C. Hedberg, L. Källström, P. I. Arvidsson, P. Brandt, P. G. Andersson, *J. Am. Chem. Soc.* 127 (2005) 15083.
- [98] X. Zhang, H. Du, Z. Wang, Y. Wu, K. Ding, *J. Org. Chem.* 71 (2006) 2862.
- [99] R. Zhu, D. Zhang, J. Wu, C. Liu, *Tetrahedron: Asymmetry* 17 (2006) 1611.

- [100] Y. Xiao, D. Jung, T. Gund, S. V. Malhotra, *J. Mol. Model.* 12 (2006) 681.
- [101] M. Bandini, A. Bottoni, P. G. Cozzi, G. P. Miscione, M. Monari, R. Pierciaccante, A. Umani-Ronchi, *Eur. J. Org. Chem.* (2006) 4596.
- [102] S. Mori, T. Vreven, K. Morokuma, *Chem. Asian J.* 1 (2006) 391.
- [103] M. Li, W. Zheng, F. Yang, A. Tian, *Int. J. Quantum Chem.* 81 (2001) 291.
- [104] A. Deiters, C. Mück-Lichtenfeld, R. Fröhlich, D. Hoppe, *Chem. Eur. J.* 8 (2002) 1833.
- [105] M. Drees, L. Kleiber, M. Weimer, T. Strassner, *Eur. J. Org. Chem.* (2002) 2405.
- [106] J. M. Fraile, J. I. Garcia, M. J. Gil, V. Martinez-Merino, J. A. Mayoral, L. Salvatella, *Chem. Eur. J.* 10 (2004) 758.
- [107] C. Costabile, L. Cavallo, *J. Am. Chem. Soc.* 126 (2004) 9592.
- [108] J. Christoffers, *Eur. J. Org. Chem.* (1998) 1259.
- [109] A. Klamt, G. Schüürmann, *J. Chem. Soc. Perkin Trans. 2* (1993) 799.
- [110] G. Scalmani, V. Barone, K. N. Kudin, C. S. Pomelli, G. E. Scuseria, M. J. Frisch, *Theor. Chem. Acc.* 111 (2004) 90.
- [111] C. Cappelli, S. Corni, B. Mennucci, R. Cammi, J. Tomasi, *J. Phys. Chem. A* 106 (2002) 12331.
- [112] R. Bonaccorsi, P. Palla, J. Tomasi, *J. Am. Chem. Soc.* 106 (1084) 1945.
- [113] C. Cappelli, S. Corni, J. Tomasi, *J. Phys. Chem. A* 105 (2001) 10807.

-
- [114] P. Bandyopadhyay, M. S. Gordon, B. Mennucci, J. Tomasi, *J. Chem. Phys.* 116 (2002) 5023.
- [115] V. Barone, M. Cossi, J. Tomasi, *J. Comput. Chem.* 19 (1998) 404.
- [116] V. Barone, M. Cossi, J. Tomasi, *J. Chem. Phys.* 107 (1997) 3210.
- [117] J. S. Bader, C. M. Cortis, B. J. Berne, *J. Chem. Phys.* 106 (1997) 2372.
- [118] T. Mineva, N. Russo, E. Sicilia, *J. Comput. Chem.* 19 (1998) 290.
- [119] R. H. Hertwig, W. Koch, *Chem. Phys. Lett.* 268 (1997) 345.
- [120] C. van Wüllen, *J. Chem. Phys.* 103 (1995) 3589.
- [121] C. van Wüllen, *J. Chem. Phys.* 105 (1996) 5485.

9 Appendix

9.1 Color code of Figures

3, 4, 5, 6, 7, 13, 16, 17, 18, 19, 20.

- purple: copper
- grey: carbon
- red: oxygen
- blue: nitrogen

9.2 Absolute energies of the calculated structures

structure	$E^{[a]}$	$E^{[b]}$	$H_{298}^{[b]}$	$G_{298}^{[b]}$
1	-345.725341	-345.603854	-345.594523	-345.637737
2	-382.395281	-382.219405	-382.208262	-382.254456
3a	-651.700114	-651.425833	-651.407753	-651.472058
3b	-769.587308	-769.228942	-769.206706	-769.280486
4	-231.181652	-231.092730	-231.086646	-231.121010
5	-576.927110	-576.711628	-576.697265	-576.752116
6a-in	-882.878225	-882.510348	-882.486334	-882.563943
6b-in	-1000.761437	-1000.308915	-1000.281085	-1000.366047
6c-in	-882.877989	-882.509522	-882.485808	-882.561849
6d-in	-1000.489022	-1000.253315	-1000.231540	-1000.302053

Table 12: Absolute energies of different minima structures: [a] electronic energy and [b] the electronic energy plus the zero point vibrational energy correction calculated with Gaussian (assumption of classical behaviour for rotation in the frequency analysis).

structure	$E^{[a]}$	$E^{[b]}$	$H_{298}^{[b]}$	$G_{298}^{[b]}$
7a	-2599.292955	-2598.900095	-2598.870293	-2598.963593
7b	-2444.514624	-2444.188055	-2444.162646	-2444.243550
$7b_4$	-2675.747091	-2675.329803	-2675.297812	-2675.396258
7c	-2520.456687	-2520.128452	-2520.103489	-2520.185635
7-triflat	-3253.371387	-3253.067263	-3253.039110	-3253.128959
$7d_4$	-2715.013935	-2714.567805	-2714.533879	-2714.635500
textbf8a	-2599.278206	-2598.884524	-2598.855320	-2598.947414
8b	-2675.723940	-2675.305907	-2675.273642	-2675.371492
8c	-2752.679493	-2751.198974	-2751.170494	-2751.255578
8d	-2714.981781	-2714.534303	-2714.502325	-2714.595730
9a	-2367.841473	-2367.551017	-2367.529460	-2367.600489
9b	-2520.478779	-2520.149746	-2520.125240	-2520.205238
9c	-2347.980911	-2347.676666	-2347.654960	-2347.728427
9d	-2407.12544	-2406.806580	-2406.784195	-2406.858099
9e	-2446.430304	-2446.083154	-2446.058596	-2446.141029

Absolute energies of different minima structures: [a] electronic energy and [b] the electronic energy plus the zero point vibrational energy correction calculated with Gaussian (assumption of classical behaviour for rotation in the frequency analysis).

structure	$E^{[a]}$	$E^{[b]}$	$H_{298}^{[b]}$	$G_{298}^{[b]}$
9f	-2484.534518	-2484.183791	-2484.158332	-2484.240294
9g	-3253.380026	-3253.076637	-3253.048625	-3253.137999
9h	-2446.431990	-2446.085214	-2446.060951	-2446.138320
9i	-2485.725466	-2485.351216	-2485.325556	-2485.405282
9j	-2525.022944	-2524.620453	-2524.594265	-2524.675152
10a	-2751.633898	-2751.212882	-2751.181813	-2751.277282
10b	-2599.278206	-2598.884524	-2598.855320	-2598.947414
10c	-2579.145228	-2578.748489	-2578.720792	-2578.805647
10d	-2638.289014	-2637.877315	-2637.848088	-2637.937402
10e	-2677.594258	-2677.153942	-2677.123641	-2677.215927
10f	-2715.697398	-2715.254497	-2715.222597	-2715.320191
10h	-2677.596064	-2677.157147	-2677.127471	-2677.216696
10i	-2716.888343	-2716.421106	-2716.389498	-2716.482826
10j	-2756.186814	-2755.692090	-2755.658578	-2755.756477
11b	-2599.010120	-2598.627166	-2598.599224	-2598.684888
11h	-2677.602874	-2677.163911	-2677.134048	-2677.223696
11i	-2716.896961	-2716.429428	-2716.397877	-2716.490083
11j	-2756.192817	-2755.697719	-2755.665147	-2755.760784

Absolute energies of different minima structures: [a] electronic energy and [b] the electronic energy plus the zero point vibrational energy correction calculated with Gaussian (assumption of classical behaviour for rotation in the frequency analysis).

transition state	$E^{[a]}$	$E^{[b]}$	$H_{298}^{[b]}$	$G_{298}^{[b]}$
TS3a/6a-in	-882.846623	-882.481353	-882.457547	-882.533884
TS3/6b-in	-1000.730305	-1000.280139	-1000.252635	-1000.335930
TS3/6c-in	-882.846978	-882.458911	-882.457967	-882.534272
TS3/6d-in	-1000.729386	-1000.280070	-1000.252267	-1000.336632
TS9a/10a	-2751.635698	-2751.216139	-2751.185374	-2751.278918
TS9b/10b	-2598.996233	-2598.614338	-2598.586900	-2598.671471
TS9c/10c	-2579.136383	-2578.741415	-2578.713581	-2578.799316
TS9d/10d	-2638.279725	-2637.869151	-2637.840258	-2637.928139
TS9e/10e	-2677.584255	-2677.145423	-2677.115210	-2677.206722
TS9f/10f	-2715.687568	-2715.245961	-2715.214288	-2715.310461
TS9h/10h	-2677.587127	-2677.148449	-2677.118602	-2677.207786
TS9i/10i	-2716.881334	-2716.414691	-2716.383731	-2716.474357
TS9j/10j	-2756.177814	-2755.683366	-2755.650654	-2755.746404
TS9b/11b	-2598.995103	-2598.614032	-2598.586117	-2598.672148
TS9h/11h	-2677.586539	-2677.149321	-2677.118642	-2677.210589
TS9i/11i	-2716.879884	-2716.414175	-2716.382648	-2716.475241
TS9j/11j	-2756.177055	-2755.684102	-2755.650545	-2755.751512

Table 13: Absolute energies of different transition states: [a] electronic energy and [b] the electronic energy plus the zero point vibrational energy correction calculated with Gaussian (assumption of classical behaviour for rotation in the frequency analysis).

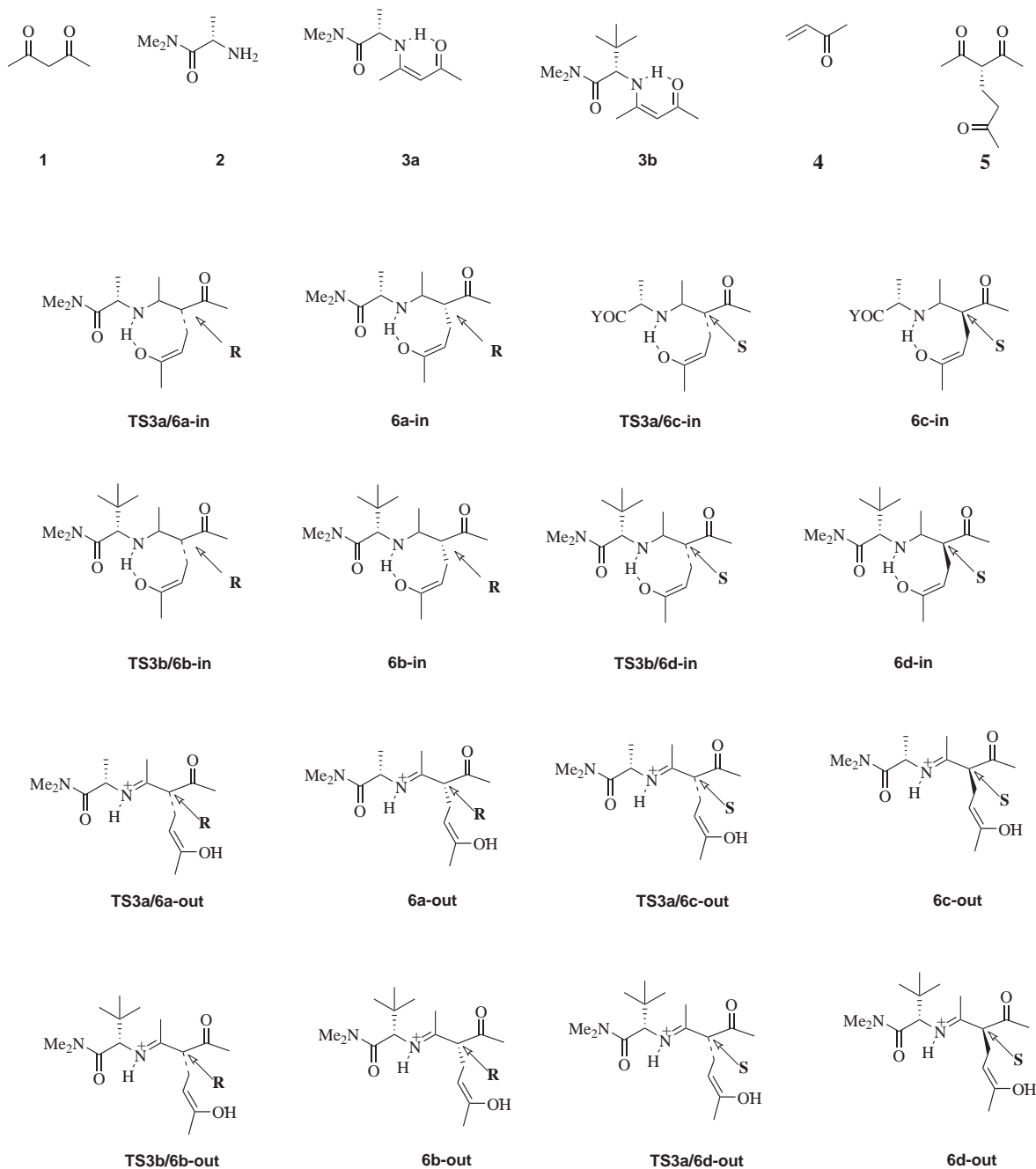
transition state	$E^{[a]}$	$E^{[b]}$	$H_{298}^{[b]}$	$G_{298}^{[b]}$
TS-outside	-2598.977947	-2598.599002	-2598.570252	-2598.660049
TS7a/8a	-2599.255244	-2598.863627	-2598.834329	-2598.924289
<i>TS7b₄8b</i>	-2675.707938	-2675.290477	-2675.258758	-2675.353606
TS7c/8c	-2751.619477	-2751.200305	-2751.169106	-2751.266201
<i>TS7d₄8d</i>	-2714.971854	-2714.525194	-2714.492992	-2714.586751
TS-alt	-2598.968932	-2598.586983	-2598.559553	-2598.644293
TS-alt-gly	-2559.697039	-2559.342983	-2559.317384	-2559.397609
TS9a/10a	-2559.694713	-2559.311399	-2559.284472	-2559.367384
TS9h/10h	-2677.655542	-2677.220764	-2677.191147	-2677.279818
TS9i/10i	-2716.948595	-2716.485409	-2716.454563	-2716.545961
TS9a/11a	-2599.063636	-2598.684617	-2598.658753	-2598.739365
TS9h/11h	-2677.651534	-2677.217457	-2677.188056	-2677.276509
TS9i/11i	-2716.943339	-2716.480287	-2716.450019	-2716.539264

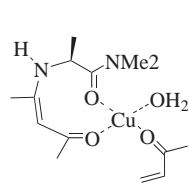
Absolute energies of different transition states: [a] electronic energy and [b] the electronic energy plus the zero point vibrational energy correction calculated with Gaussian (assumption of classical behaviour for rotation in the frequency analysis).

structure	TZVP basis set	SVP/SV basis set
7a	-2599.292955	-2598.635222
TS7a/8a	-2599.255244	-2598.597527
TS9i/10i	-2716.881334	-2716.608151
TS9i/11i	-2716.879884	-2716.606621

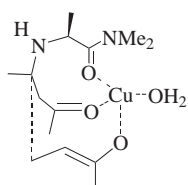
Table 14: Reduction of calculation time: Absolute energies in Hartree using the TZVP and the and SVP/SV basis set for two reaction pathways

9.3 Overview of the calculated structures

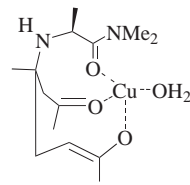




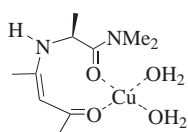
7a



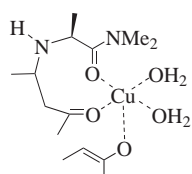
TS7a/8a



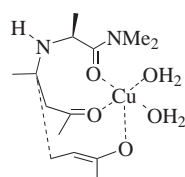
8a



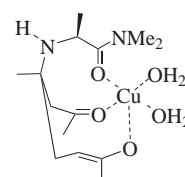
7b



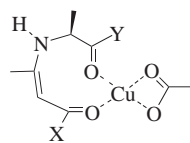
7b4



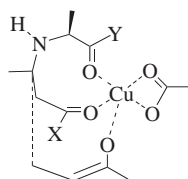
TS7b4/8b



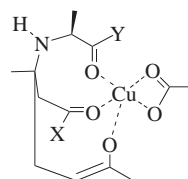
8b



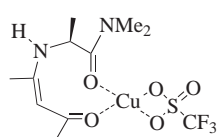
7c



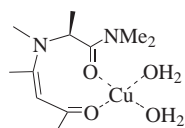
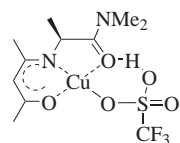
TS7c/8c



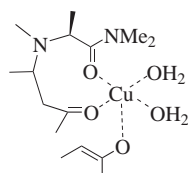
8c



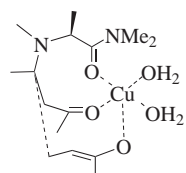
7triflat



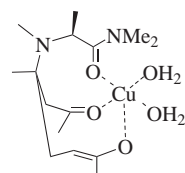
7d



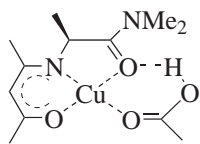
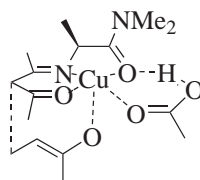
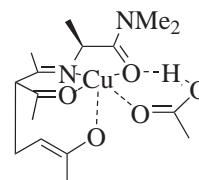
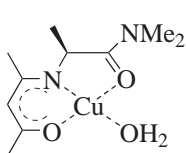
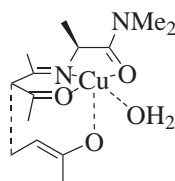
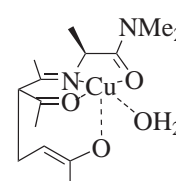
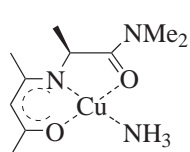
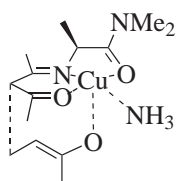
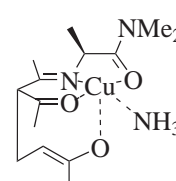
7d4

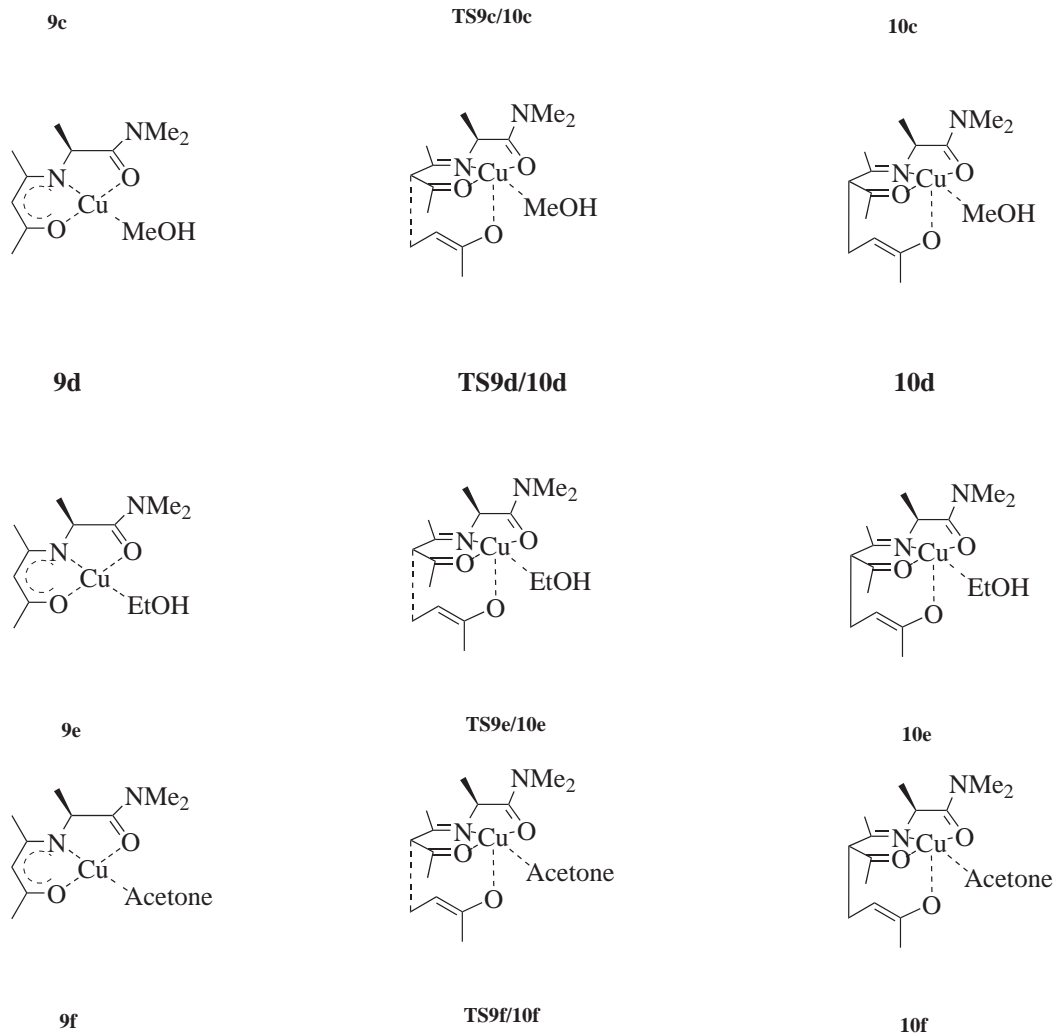


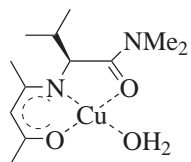
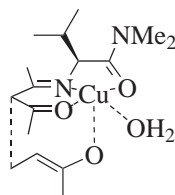
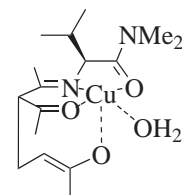
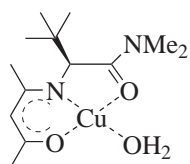
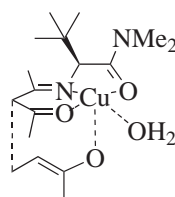
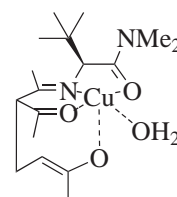
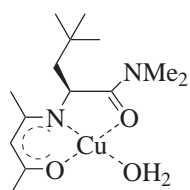
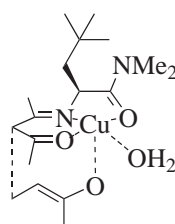
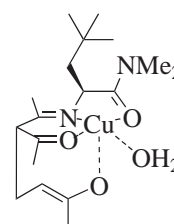
TS7d4/8d

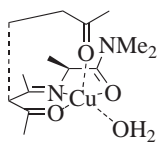


8b

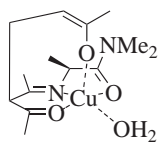
**9a****TS9a/10a****10a****9b****TS9b/10b****10b****9c****TS9c/10c****10c**



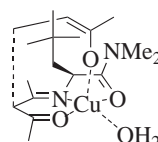
**9h****TS9h/10h****10h****9i****TS9i/10i****10i****9j****TS9j/10j****10j**



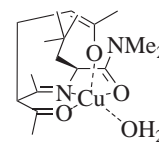
TS9b/11b



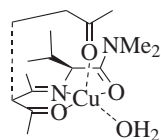
11b



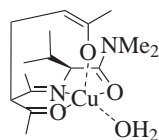
TS9j/11j



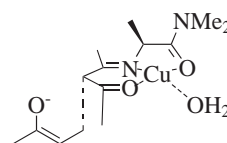
11j



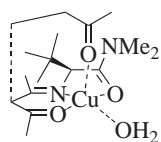
TS9h/11h



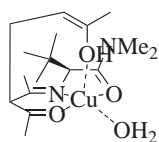
11h



TS-outside



TS9i/11i



11i

9.4 List of Publications

- Julia Borowka and Christoph van Wüllen
Computational studies on the copper(II) catalyzed Michael reaction
J. Organomet. Chem. (691), 4474–4479, **2006**